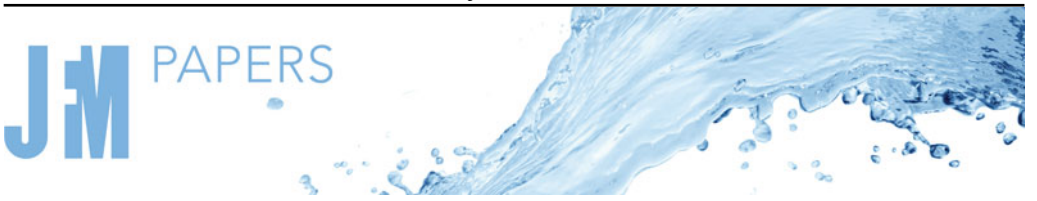
J. Fluid Mech. (2026), *vol.* 1040, A49, doi:10.1017/jfm.2026.11908



Falling dynamics of flexible plates with concentrated weight

Junqi Xiong[1,2], **Kui Liu**[1], **Zhi-Qiang Dong**[2,3] and **Haibo Huang**[1]

[1]Department of Modern Mechanics, University of Science and Technology of China, Hefei, Anhui 230026, PR China

[2]Advanced Institute for Ocean Research, Southern University of Science and Technology, Shenzhen, Guangdong 518055, PR China

[3]Department of Mechanics and Aerospace Engineering, Southern University of Science and Technology, Shenzhen, Guangdong 518055, PR China

Corresponding author: Haibo Huang, huanghb@ustc.edu.cn

(Received 28 January 2026 UTC; revised 23 May 2026 UTC; accepted 9 July 2026 UTC)

We investigate the free fall of a flexible plate with a concentrated central weight using numerical simulations to explore the coupling effects of structural flexibility and concentrated loading. Two-dimensional and three-dimensional (3-D) simulations, combining lattice Boltzmann and immersed boundary methods, identify four distinct falling modes: swing, stable falling, fluttering and tumbling. The swing and stable falling modes are reported for the first time in this context. By analysing the balance between bending stiffness K and concentrated weight G, we introduce a new dimensionless effective stiffness $Kg = K/G$, which governs mode transitions and successfully collapses the kinematic data. A bistable transition zone between fluttering and tumbling is observed, with the mode selection dependent on the initial inclination angle, which scales as a power law of Kg. Additionally, within the swing mode, we observe a transition in wake topology from a 2P to a 2S vortex-shedding pattern, modulated by the mass ratio. In 3-D simulations, the finite aspect ratio A_r significantly influences mode selection due to pressure leakage at the side edges. While the Kg scaling remains valid for the global dynamics, 3-D effects suppress tumbling in narrow plates and induce spanwise oscillations in the stable falling mode at higher aspect ratios.

Key words: flow-structure interactions, vortex interactions

https://doi.org/10.1017/jfm.2026.11908 Published online by Cambridge University Press

© The Author(s), 2026. Published by Cambridge University Press.

1. Introduction

Falling bodies in fluid, from drifting autumn leaves to coins dropped in water, have long fascinated scientists. Their trajectories and stability arise from fluid–structure interaction (FSI), where inertial, viscous and elastic forces (when present) compete to dictate motion. A classic example is the descent of a plate-like body in air: by perturbing the surrounding fluid, it creates a pressure difference between its upper and lower surfaces, generating lift that sustains a passive flight state. Passive flight is widely observed in nature, with plant seeds using rotation or oscillation to slow descent and extend dispersal distances, and spiders using flexible silk threads to migrate in the wind. Understanding the mechanisms behind passive flight is crucial for both fundamental fluid mechanics and biomimetic design, such as micro-air vehicles.

Theoretical studies of falling plates date back to Maxwell (1852), who identified the critical role of the relative locations of the centre of gravity and centre of pressure. Subsequent research, such as the landmark experiments by Willmarth *et al.* (1964), mapped the flight modes in terms of Reynolds number Re and dimensionless moment of inertia I^*, showing that heavier bodies tend to tumble, while lighter ones flutter. More recent studies have refined this picture, demonstrating that transitions between these states can be chaotic and governed by a low-dimensional dynamics (Field *et al.* 1997; Andersen *et al.* 2005). While much attention has been given to rigid bodies, introducing structural flexibility fundamentally enriches the problem. Alben (2010) demonstrated that flexibility can alter the flight state of a falling sheet, with experiments by Tam (2015) showing that flexible wings can enhance lift and prolong flight by storing and releasing elastic energy. Lau & Huang (2021) further explored how varying flexibility in a viscous fluid yields distinct descent patterns, establishing flexibility as a key control parameter for passive flight.

A particularly interesting case is the 'winged seeds' of plants, such as those in the *Dipterocarpaceae* family. Unlike uniform sheets, these seeds feature a heavy, concentrated mass at the centre or leading edge, supported by a lightweight, flexible wing. Rabault *et al.* (2019) demonstrated that the curvature and mass distribution of such seeds are optimised for slow descent, while Vincent *et al.* (2020) showed that non-uniform flexibility in a tumbling wing can improve flight efficiency by reducing drag. Despite these advances, the specific interaction between a concentrated weight and a flexible membrane remains underexplored in the context of passive flight.

The wake of a falling body, or the pattern of vortices it sheds, is closely linked to its descent dynamics. For example, a heavy disk or sphere descending almost vertically typically produces a classic Kármán vortex street (2S shedding pattern, i.e. two single vortices per cycle). When conditions change, the wake can transition to a 2P mode (two pairs of vortices per cycle), typically coinciding with larger-amplitude planar oscillations of the body. Previous studies (Mathai *et al.* 2017) showed that the transition from 2S to 2P shedding in falling bodies is governed by factors like the mass ratio and moment of inertia. Understanding this interplay between vortex shedding and motion is key to explaining the transitions between fluttering, tumbling or spiralling behaviours.

Most previous studies on falling plates have considered either rigid bodies with prescribed geometry and mass distribution, or flexible sheets and plates whose weight and inertia are distributed over the entire body. In these systems, mode selection is usually discussed in terms of Reynolds number, moment of inertia and overall flexibility. The centrally weighted flexible plate considered here is mechanically different: the gravitational driving force is localised at the centre, whereas the elastic restoring force and hydrodynamic loading are distributed along the deformable plate. This separation

https://doi.org/10.1017/jfm.2026.11908 Published online by Cambridge University Press

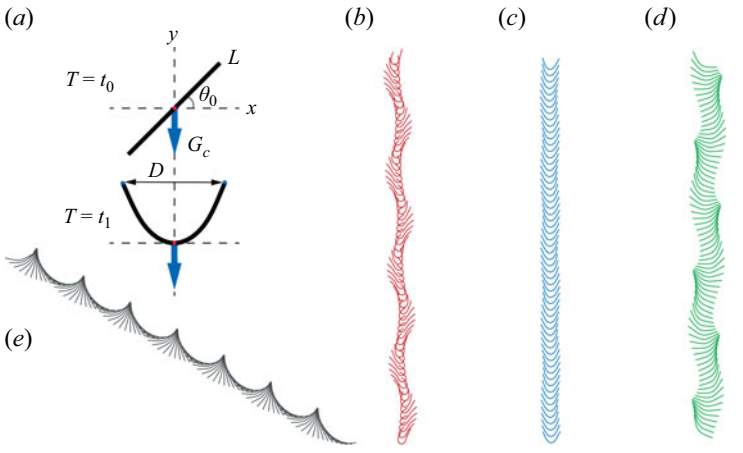


Figure 1. (*a*) Schematic illustration of a 2-D flexible plate falling under a concentrated weight G_c. Two instants are shown: at $T = t_0$, the plate remains undeformed with the initial inclination angle θ_0; at $T = t_1$, the plate bends as it descends, representing a typical instantaneous falling configuration. (*b*–*e*) Representative falling modes observed in simulations: (*b*) swing, (*c*) stable falling, (*d*) fluttering and (*e*) tumbling.

between localised forcing and distributed deformation creates a distinct FSI problem, relevant to lightweight flexible wings or winged-seed-like structures carrying a compact mass. It also gives rise to falling regimes that are absent or not emphasised in previous uniformly weighted flexible-plate studies, including the swing and stable falling modes.

Motivated by this physical distinction, we systematically perform numerical simulations of the free fall of a flexible plate driven by a concentrated central weight in both two-dimensional (2-D) and three-dimensional (3-D) scenarios. We map the flight dynamics and identify four distinct descent modes: swing, stable falling, fluttering and tumbling. To capture the underlying physics, we introduce the effective stiffness $Kg = K/G$, which quantifies the competition between bending stiffness and concentrated gravitational loading, and use it to accurately organise the mode transitions and collapse the kinematic data. Additionally, we explore a bistability phenomenon at the fluttering–tumbling transition dependent on the initial inclination angle, and investigate vortex-shedding transitions within the swing mode. In 3-D simulations, we examine finite-span effects and reveal new flight behaviours, such as spanwise oscillations in wide plates. These findings offer new insights into the passive flight of non-uniformly weighted structures, with potential applications in micro-air vehicles and the dispersal of plant seeds.

The paper is organised as follows: the physical problem and mathematical formulation are described in § 2, the numerical method and verification are detailed in § 3, the results are discussed in § 4 and concluding remarks are provided in § 5.

2. Physical problem and mathematical formulations

As illustrated in figure 1(*a*), we consider the sedimentation of a 2-D flexible plate of length L in an initially quiescent fluid, driven solely by a weight $G_c = m_c g$ concentrated at the centre of the plate, where m_c is the concentrated mass and g is the magnitude of gravitational acceleration $\boldsymbol{g}$. In the 3-D cases, we consider plates with different span widths W. The concentrated weight G_c is uniformly distributed along the spanwise centreline of the plate, corresponding to the row of mid-chord nodes indicated by the red line in figure 2. The gravitational force acting on the rest of the plate is neglected.

https://doi.org/10.1017/jfm.2026.11908 Published online by Cambridge University Press

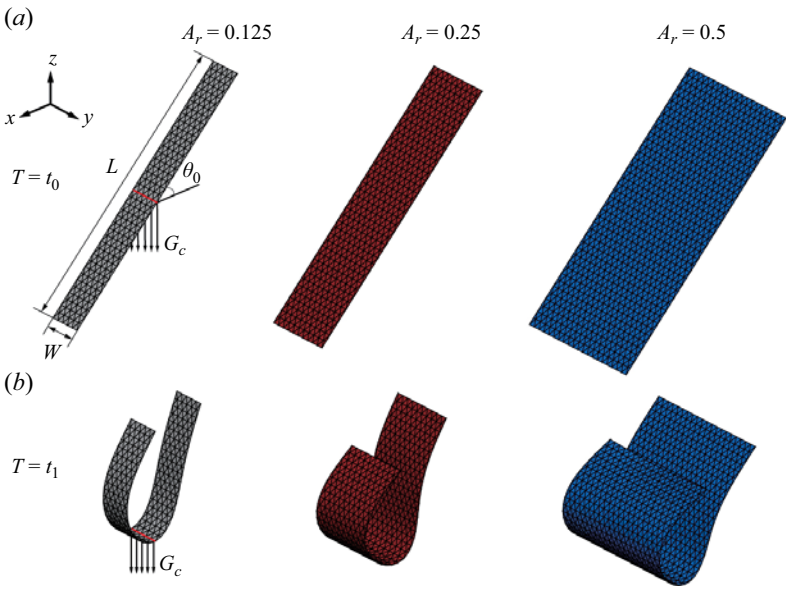


Figure 2. Schematic of the 3-D flexible plate: (*a*) initial configuration and (*b*) a snapshot during descent. Here, L and W denote the chord length and span width, respectively, and $A_r = W/L$ is the aspect ratio. The concentrated weight G_c is uniformly distributed along the nodes indicated by the red line. The initial inclination angle is θ_0.

This configuration abstracts practical FSI systems where a lightweight flexible membrane or wing carries a heavily localised payload, such as winged seeds (e.g. samara) during passive dispersal or micro-air vehicles with a central mass. To rigorously justify the validity of neglecting the distributed self-weight of the lightweight plate, a comprehensive sensitivity analysis is provided in Appendix A, which confirms that its inclusion yields negligible quantitative corrections to the macroscopic kinematics and mode transitions. The governing equations for the flow are the Navier–Stokes equations

$$\frac{\partial \boldsymbol{v}}{\partial t} + \boldsymbol{v} \cdot \nabla \boldsymbol{v} = -\frac{1}{\rho}\nabla p + \frac{\mu}{\rho}\nabla^2 \boldsymbol{v} + \boldsymbol{f}, \tag{2.1}$$

$$\nabla \cdot \boldsymbol{v} = 0, \tag{2.2}$$

where ρ is the fluid density, $\boldsymbol{v}$ is the velocity, p is the pressure, μ is the dynamic viscosity and $\boldsymbol{f}$ represents the body force exerted by the immersed boundary on the surrounding fluid.

The Euler–Bernoulli beam equation is adopted to resolve the deformation and kinematics of the flexible plate

$$\rho_s h \frac{\partial^2 \boldsymbol{X}}{\partial t^2} = \sum_{i,j=1}^{2} \frac{\partial}{\partial s_i}\left\{\varphi_{ij}\left[\delta_{ij} - \left(\frac{\partial \boldsymbol{X}}{\partial s_i}\cdot\frac{\partial \boldsymbol{X}}{\partial s_j}\right)^{-1/2}\right]\frac{\partial \boldsymbol{X}}{\partial s_j} - \frac{\partial}{\partial s_j}\left(\gamma_{ij}\frac{\partial^2 \boldsymbol{X}}{\partial s_i \partial s_j}\right)\right\} + \boldsymbol{F}_s + \boldsymbol{F}_c + \boldsymbol{F}_g, \tag{2.3}$$

where $\boldsymbol{X}(s_1, s_2, t) = (X, Y, Z)$ denotes the position vector of the plate, where s_1 and s_2 are the Lagrangian coordinates in the chordwise and spanwise directions, respectively. The density and thickness of the plate are given by ρ_s and h. The term $\boldsymbol{F}_s$ represents the Lagrangian force exerted by the surrounding fluid, $\boldsymbol{F}_c$ is the repulsive force to avoid

https://doi.org/10.1017/jfm.2026.11908 Published online by Cambridge University Press

contact and overlap between plate elements and $\boldsymbol{F}_g = G_c\boldsymbol{g}/g$ is the weight added at the centre of the plate. The in-plane stiffness tensor is defined as φ_{ij}, with $\varphi_{11} = \varphi_{22} = \varphi$ being the stretching stiffness and $\varphi_{12} = \xi$ the shearing stiffness. The bending stiffness is characterised by the out-of-plane effect matrix γ_{ij}, where $\gamma_{11} = \gamma$. Here, δ_{ij} represents the Kronecker delta. The boundary conditions at all edges are

$$\varphi_{ij}\left[\delta_{ij} - \left(\frac{\partial \boldsymbol{X}}{\partial s_i}\cdot\frac{\partial \boldsymbol{X}}{\partial s_j}\right)^{-1/2}\right]\frac{\partial \boldsymbol{X}}{\partial s_j} - \frac{\partial}{\partial s_j}\left(\gamma_{ij}\frac{\partial^2 \boldsymbol{X}}{\partial s_i \partial s_j}\right) = 0, \quad \frac{\partial^2 \boldsymbol{X}}{\partial s_i \partial s_j} = 0. \tag{2.4}$$

Note that the Einstein summation convention is suppressed for indices i and j ($i, j = 1, 2$).

The dynamics of a 2-D flexible plate can be described using a simplified equation (2.3)

$$\rho_s h\frac{\partial^2 \boldsymbol{X}}{\partial t^2} - \frac{\partial}{\partial s}\left[\varphi\left(1 - \left|\frac{\partial \boldsymbol{X}}{\partial s}\right|^{-1}\right)\frac{\partial \boldsymbol{X}}{\partial s}\right] + \gamma\frac{\partial^4 \boldsymbol{X}}{\partial s^4} = \boldsymbol{F}_s + \boldsymbol{F}_c + \boldsymbol{F}_g. \tag{2.5}$$

The short-range repulsive force $\boldsymbol{F}_c$ is calculated following the formulation of Huang *et al.* (2007)

$$\boldsymbol{F}_c(s,t) = \int_0^L \delta\left(\boldsymbol{X}(s,t) - \boldsymbol{X'}\left(s',t\right)\right)\frac{\boldsymbol{X} - \boldsymbol{X'}}{\left|\boldsymbol{X} - \boldsymbol{X'}\right|}\mathrm{d}s', \tag{2.6}$$

where $\boldsymbol{X}(s,t)$ and $\boldsymbol{X}(s',t)$ denote the position vectors of the interacting segments. The term δ represents the three-point discrete delta function described by Wang & Zhang (2011).

The characteristic quantities density ρ, length L and velocity $U_{ref} = \mu\chi/\rho L$ are chosen to normalise the above equations. Here, ρ, L and μ are fixed, and $\chi = 200$ serves purely as a numerical scaling factor. It positions the *a priori* reference velocity U_{ref} within a moderate range to satisfy the low-Mach-number constraint required by the lattice Boltzmann method, leaving the underlying FSI physics entirely invariant. Therefore, the characteristic time is $T_{ref} = L/U_{ref}$, the characteristic force is $F_{ref} = (1/2)\rho U_{ref}^2 L$ and the gravitational acceleration is $g = U_{ref}^2/L$. Based on dimensional analysis, the key non-dimensional parameters are listed as follows: the aspect ratio $A_r = W/L$, the Reynolds number $Re = \rho U_d L/\mu$, the mass ratio of the plate to the fluid $M = \rho_s h/\rho L$, the dimensionless concentrated weight at the centre of the plate $G = G_c/F_{ref}$, the dimensionless stretching stiffness $S = \varphi/\rho U_{ref}^2 L$ and the dimensionless bending stiffness $K = \gamma/\rho U_{ref}^2 L^3$. Here, Re is evaluated *a posteriori* using the measured mean settling speed U_d.

3. Numerical method and verification

3.1. *Numerical method*

The governing equations (2.1) and (2.2) for the flow are solved by the lattice Boltzmann method (Chen & Doolen 1998), while the deformation equation (2.3) of the flexible plate is solved by the finite element method (Doyle 2013). The immersed boundary method (Peskin 2002; Iaccarino & Mittal 2005) is adopted to couple the fluid and structure solvers. The Lagrangian force $\boldsymbol{F}_s$ between the fluid and flexible plate can be calculated by the penalty scheme (Goldstein *et al.* 1993)

$$\boldsymbol{F}_s = \alpha\int_0^t\left[\boldsymbol{V}_f\left(s,t'\right) - \boldsymbol{V}_s\left(s,t'\right)\right]\mathrm{d}t' + \beta\left[\boldsymbol{V}_f(s,t) - \boldsymbol{V}_s(s,t)\right], \tag{3.1}$$

https://doi.org/10.1017/jfm.2026.11908 Published online by Cambridge University Press

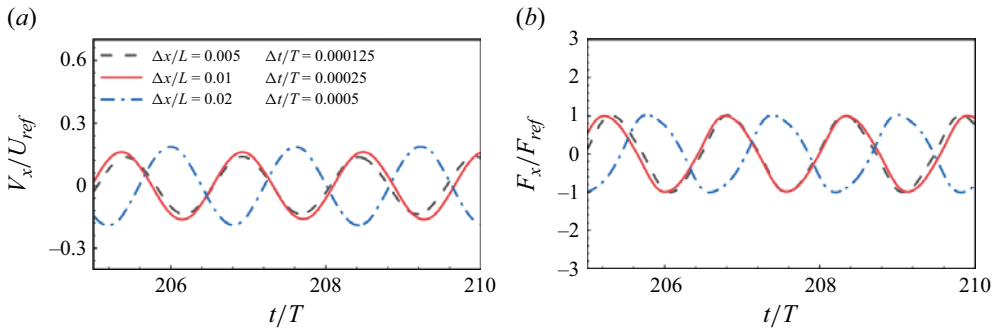


Figure 3. Grid and time-step independence study for 2-D cases: (*a*) the normalised horizontal velocity V_x of the plate's centre as a function of time and (*b*) the normalised streamwise force F_x as a function of time. In all cases, $G = 6$, $M = 1$, $K = 0.005$.

where α and β are penalty parameters chosen in accordance with prior studies (Huang *et al.* 2018; Peng *et al.* 2018; Zhang *et al.* 2020; Xu *et al.* 2022). The structural velocity at each Lagrangian point is denoted by $\boldsymbol{V}_s = \partial \boldsymbol{X}/\partial t$, while the fluid velocity $\boldsymbol{V}_f$ is obtained by interpolation

$$\boldsymbol{V}_f(s, t) = \int \boldsymbol{v}(\boldsymbol{x}, t)\delta(\boldsymbol{x} - \boldsymbol{X}(s, t))\mathrm{d}\boldsymbol{x}. \tag{3.2}$$

By applying the Dirac delta function, the body force $\boldsymbol{f}$ on the Eulerian points is

$$\boldsymbol{f}(\boldsymbol{x}, t) = -\int \boldsymbol{F}_s(s, t)\delta(\boldsymbol{x} - \boldsymbol{X}(s, t))\mathrm{d}s. \tag{3.3}$$

The numerical strategy has been successfully applied to a wide range of FSI problems, particularly in the study of flexible plates, such as tandem flexible inverted flags in a uniform flow (Huang *et al.* 2018), the influence of the trailing-edge shape on the propulsion efficiency of heaving flexible plates (Zhang *et al.* 2020) and the dynamics of the weighted flexible ribbons in a uniform flow (Liu & Huang 2024).

Dirichlet boundary conditions with $\boldsymbol{v} = 0$ are applied to the top and bottom boundaries, and Neumann boundary conditions with $\partial \boldsymbol{v}/\partial n = 0$ are imposed on the left and right. To minimise boundary effects, simulations are conducted in computational domains of $[-20, 20] \times [-20, 20]$ for 2-D cases and $[-10, 10] \times [-10, 10] \times [-2, 15]$ for 3-D cases. A moving mesh strategy is used to keep the plate centred, optimising computational efficiency.

To verify grid and time-step independence, we test three sets of $\Delta x/L$ and $\Delta t/T$ for the simulations. For the 2-D cases (figure 3), the results for the medium spatial and temporal resolution ($\Delta x/L = 0.01$, $\Delta t/T = 0.00025$) align closely with those of the finest resolution ($\Delta x/L = 0.005$, $\Delta t/T = 0.000125$). The coarsest 2-D result shows a visible phase drift after many oscillation cycles; this drift is caused by the accumulation of a small frequency mismatch and should not be interpreted as an observed convergence order. The close agreement between the medium and fine resolutions in amplitude, period and phase confirms that $\Delta x/L = 0.01$ and $\Delta t/T = 0.00025$ are sufficient for the present 2-D simulations. For the 3-D cases (figure 4), the results for $\Delta x/L = 0.025$ and $\Delta t/T = 0.000625$ match those obtained with the finest resolution, confirming grid and time-step independence for these values.

https://doi.org/10.1017/jfm.2026.11908 Published online by Cambridge University Press

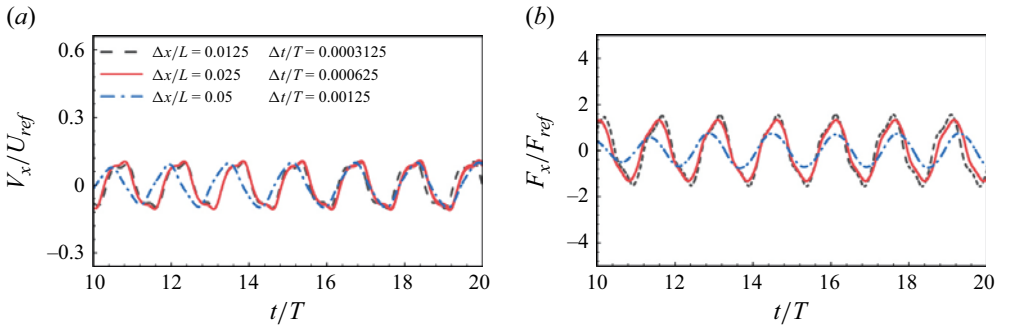


Figure 4. Grid and time-step independence study for 3-D cases: (*a*) the normalised horizontal velocity V_x of the plate's centre as a function of time and (*b*) the normalised streamwise force F_x as a function of time. In all cases, $G = 6$, $M = 1$, $K = 0.005$ and $A_r = 0.125$.

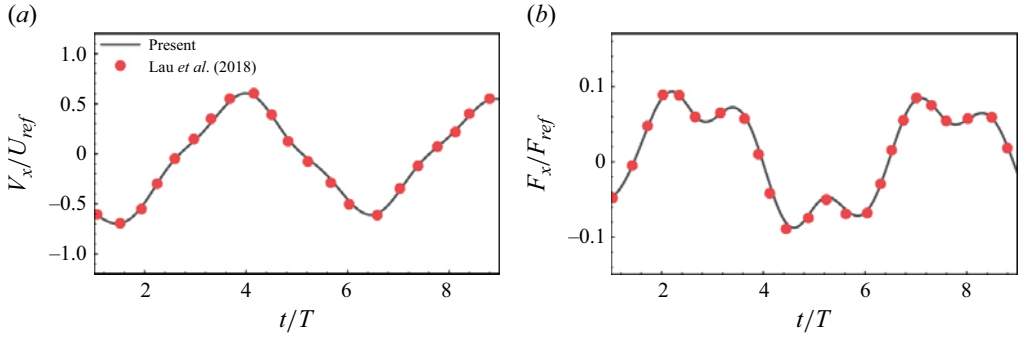


Figure 5. Verification for cases: (*a*) time evolution of the normalised horizontal velocity V_x of the plate centre and (*b*) the corresponding normalised fluid force in the streamwise direction F_x. In all cases, $Re = 80$, $I^* = 0.1$ and $K = 50$.

3.2. *Verification*

To verify our numerical method, we consider the falling plate problem in the 2-D case. The dimensionless parameters are set as $Re = 80$, $K = 50$ and $I^* = 0.1$, where $I^* = 8\rho^* h^*(1 + h^*)/3\pi$ is the dimensionless moment of inertia, $\rho^* = \rho_s/\rho$ is the density ratio of the plate to the fluid and $h^* = h/L$ is the thickness ratio of the plate. Figures 5(*a*) and 5(*b*) show the transverse velocity of the plate's centre and the corresponding lateral force exerted by the surrounding fluid, respectively. The results exhibit good agreement with the numerical solution derived by Lau *et al.* (2018).

For the case of a uniform flexible plate, previous studies have identified three typical modes: tumbling, chaotic and fluttering (Lau & Huang 2021). To assess the distribution of these modes in the (Re, I^*) phase space, we performed a highly dense parameter sampling, particularly focusing on the critical transition boundaries. As shown in figure 6, the refined boundaries and the mode distributions exhibit excellent agreement with the numerical data reported by Lau & Huang (2021), thereby validating the accuracy and reliability of our FSI framework.

4. Results and discussion

In all simulations, the plate is initially released from rest and settles under the concentrated weight. To systematically investigate the falling dynamics, the key dimensionless

https://doi.org/10.1017/jfm.2026.11908 Published online by Cambridge University Press

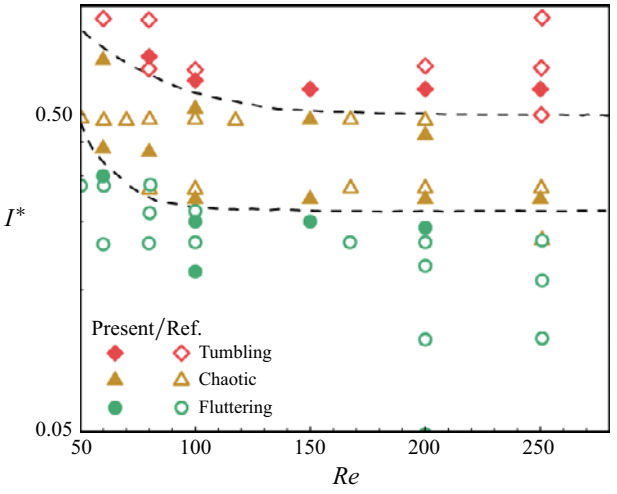


Figure 6. Phase diagram of the three typical falling modes in the (Re, I^*) parameter space. Open symbols denote the numerical results of Lau & Huang (2021), while solid symbols represent the present simulation results. In all cases, $K = 0.05$.

parameters are varied within representative ranges: the concentrated weight is selected in the range of $G \in [2, 6]$, a span chosen to ensure sufficient structural deformation for flexible modes to emerge while preventing excessive distortion. The bending stiffness covers a wide spectrum from highly flexible ($K = 0.001$) to quasi-rigid ($K = 1$) regimes, and the mass ratio M is investigated within [0.1, 1.0]. The *a posteriori* analysis confirms that the resulting Reynolds number Re falls within the range of 200 to 700, which is consistent with the flow regimes reported in previous studies on falling plates (Lau *et al.* 2018).

In most 2-D cases, the final falling mode is independent of the initial inclination angle θ_0. Unless otherwise noted, $\theta_0 = 45°$ is used to expedite the transition to quasi-steady falling. It is noticed that the initial angle only affects cases near the fluttering–tumbling boundary when $\theta_0 > 75°$. The influence of θ_0 on falling modes is discussed in § 4.1.3. For 3-D cases, the final falling mode is insensitive to θ_0. The stretching stiffness is set to $S = 10^4$ to keep the plate nearly inextensible. The mass ratio M is constant at $M = 1.0$, except when discussed in §§ 4.1.4 and 4.2.2.

4.1. *Two-dimensional cases study*

4.1.1. *Four falling modes and characteristics*

In 2-D simulations, with $A_r = \infty$, we investigate the four falling modes under a concentrated weight, shown in figure 1($b - e$):

(i) Swing: driven by the concentrated weight, the plate adopts a 'U' shape. The two lateral arms of the plate flap reciprocally, resembling flapping wings, while the plate as a whole undergoes small-amplitude, symmetric periodic swinging along the vertical centreline, akin to a pendulum.

(ii) Stable falling: following a large symmetric deformation, the plate locks into a static posture, descending vertically as a stable 'U' shape. This mode is characterised by the absence of lateral drift or angular oscillation.

https://doi.org/10.1017/jfm.2026.11908 Published online by Cambridge University Press

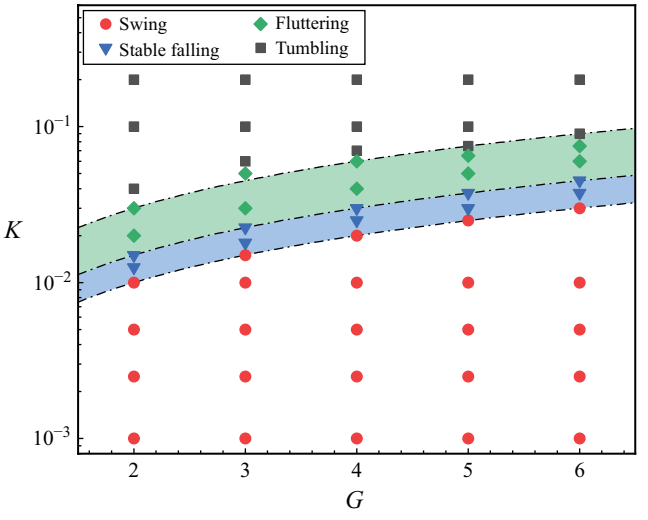


Figure 7. Phase diagram of the plate falling modes in the (G, K) parameter space. The black dash-dotted lines indicate specific values of K/G, delineating the boundaries between different modes. The blue-shaded region denotes the regime where the stable falling mode occurs, while the green-shaded region represents the bistable zone.

(iii) Fluttering: the plate exhibits the classic zigzag trajectory, accompanied by periodic oscillations in attitude angle and significant lateral reciprocating drift. This mode involves coupled deformation of the flexible tips.
(iv) Tumbling: the plate continuously rotates in one direction about its axis, breaking the left–right symmetry and causing a significant unidirectional lateral drift during its descent.

While fluttering and tumbling are well-documented modes, swing and stable falling are newly identified here. The two governing parameters are the concentrated weight G and bending stiffness K. As shown in figure 7, we observe a transition from swing to stable falling, fluttering and finally tumbling modes as K increases. The swing mode dominates for low K ($K < 0.01$), and tumbling occurs for high K ($K > 0.1$). The stable falling and fluttering modes act as transitional states. Notably, the transition boundaries are marked by the ratio K/G, motivating the dimensionless parameter discussed in § 4.1.2. The green-shaded region marks a bistable zone near the fluttering–tumbling boundary, where the falling mode may depend on the initial inclination θ_0.

Figure 8 presents detailed instantaneous flow structures and force distributions for four representative modes, and figure 9 shows the corresponding vorticity fields at the same instants. Here, the force $\boldsymbol{F}_s$ acting on the plate from the surrounding fluid can be decomposed into two components: the tangential force $\boldsymbol{F}_\tau$, arising from viscous effects, and the normal force $\boldsymbol{F}_n$, driven by the pressure difference. Their mathematical formulations are given by

$$\boldsymbol{F}_s = \left[-p\boldsymbol{I} + \boldsymbol{T}_\mu\right] \cdot n = \boldsymbol{F}_\tau + \boldsymbol{F}_n, \tag{4.1}$$

$$\boldsymbol{F}_\tau = (\boldsymbol{F}_s \cdot \boldsymbol{\tau})\, \boldsymbol{\tau} = f_\tau \boldsymbol{\tau} = \left(f_{\tau,x},\, f_{\tau,y}\right), \tag{4.2}$$

$$\boldsymbol{F}_n = (\boldsymbol{F}_s \cdot \boldsymbol{n})\, \boldsymbol{n} = f_n \boldsymbol{n} = \left(f_{n,x},\, f_{n,y}\right), \tag{4.3}$$

https://doi.org/10.1017/jfm.2026.11908 Published online by Cambridge University Press

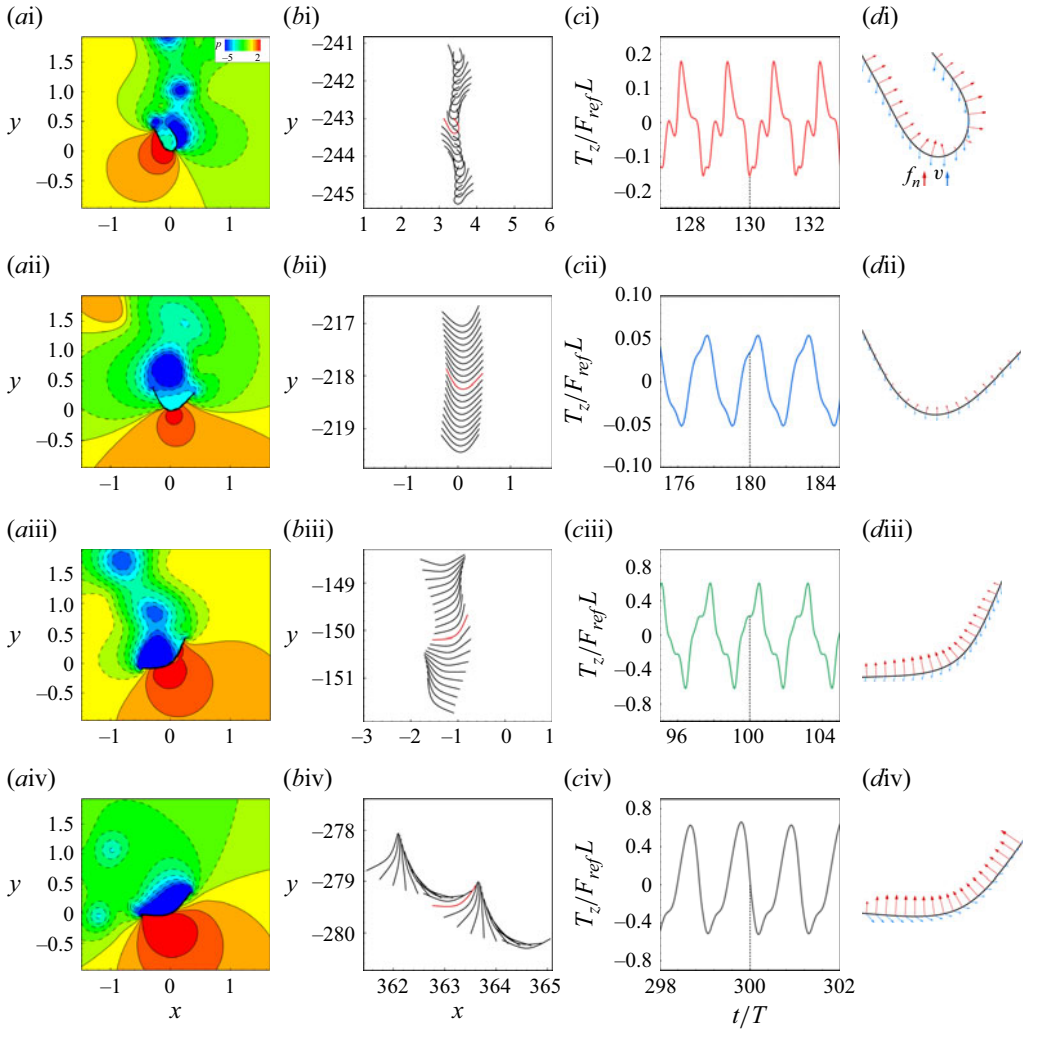


Figure 8. Detailed flow and force/torque analysis for the four typical falling modes: (i) swing ($G = 3$, $K = 0.01$), (ii) stable falling ($G = 2$, $K = 0.015$), (iii) fluttering ($G = 5$, $K = 0.07$) and (iv) tumbling ($G = 5$, $K = 0.09$). Column (a) displays the instantaneous pressure contours p around the falling plate. Column (b) shows the trajectories of the plate centre and shape evolution. Column (c) plots the time histories of the normalised hydrodynamic torque T_z evaluated with respect to the centre of mass. Column (d) presents the distribution of the normal fluid force f_n acting on the plate surface at the selected instants (red arrows), with superimposed velocity vectors (blue arrows). The specific instants visualised in columns (a) and (d) are denoted by the red curves in column (b) and the vertical black dashed lines in column (c).

in which $\boldsymbol{\tau}$ and $\boldsymbol{n}$ denote the unit tangential and normal vectors at the Lagrangian node, respectively, $\boldsymbol{T}_\mu$ represents the viscous stress tensor, while $\boldsymbol{I}$ is the identity tensor. The normal force f_n is dominated by the pressure difference across the plate, with the tangential force f_τ being negligible in our analysis, as its magnitude is orders of magnitude smaller. We focus on the magnitude and distribution of f_n since the plate's motion and deformation are driven by this force.

To further quantify the structural rotation and provide a deeper mechanistic understanding of the mode transitions, the hydrodynamic torque $T_z(t)$ acting on the

https://doi.org/10.1017/jfm.2026.11908 Published online by Cambridge University Press

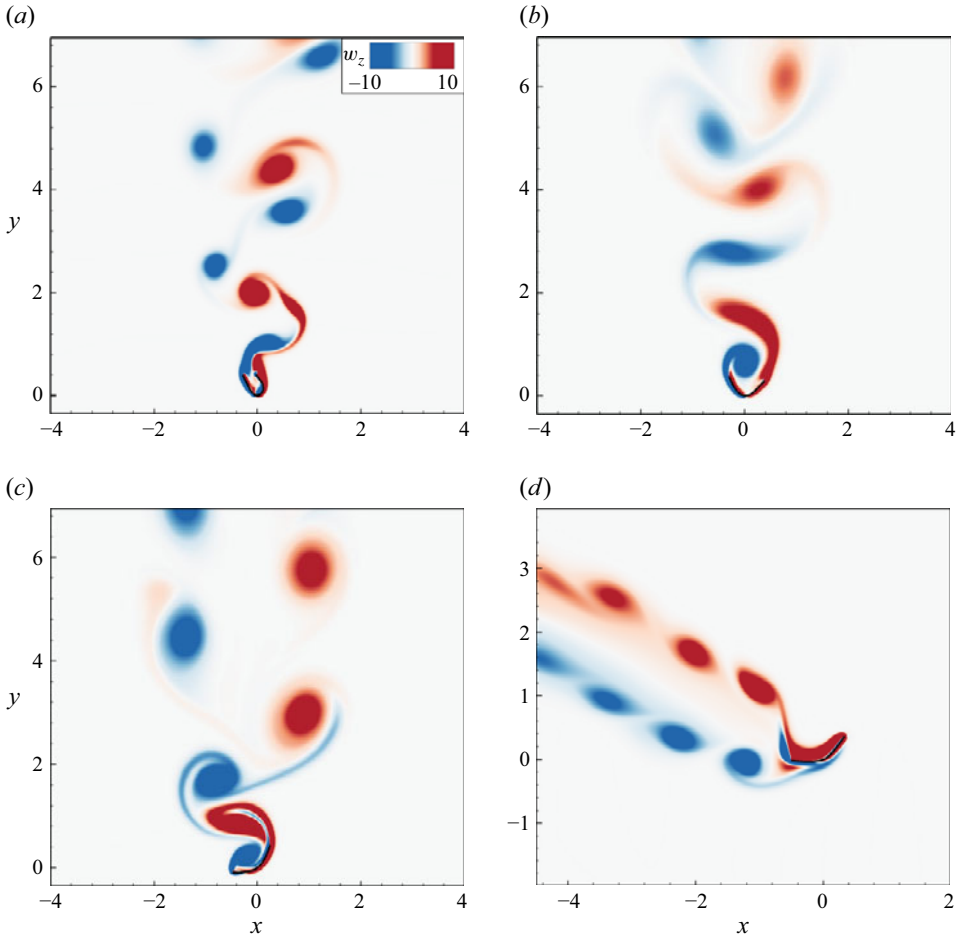


Figure 9. Instantaneous vorticity contours (ω_z) for the four typical falling modes, corresponding to the red curves shown in figure 8: (*a*) swing mode, (*b*) stable falling mode, (*c*) fluttering mode and (*d*) tumbling mode.

flexible plate, evaluated with respect to its instantaneous centre of mass $\boldsymbol{X}_{com}(t)$, is introduced and defined as

$$T_z(t) = \int_0^L [(\boldsymbol{X}(s,t) - \boldsymbol{X}_{com}(t)) \times \boldsymbol{F}_s(s,t)] \cdot \boldsymbol{k}\, \mathrm{d}s, \tag{4.4}$$

where $\boldsymbol{k}$ is the unit vector perpendicular to the 2-D motion plane. It should be explicitly noted that all flow snapshots, trajectories and force/torque characteristics analysed below are extracted from the fully developed, asymptotic quasi-steady or limit-cycle regime, long after the initial transient effects have completely dissipated.

The hydrodynamic mechanisms for each falling mode are as follows:

(i) Swing: at low K, the plate bends passively due to the concentrated weight and load of fluid. The pressure field (figure 8*a*i) shows a high-pressure zone on one arm and a low-pressure zone on the other, causing lateral force and a restoring moment (figure 8*a*iv). As reflected in the torque history (figure 8*a*iii), this restoring mechanism produces a symmetric, periodic torque alternating about zero. This

https://doi.org/10.1017/jfm.2026.11908 Published online by Cambridge University Press

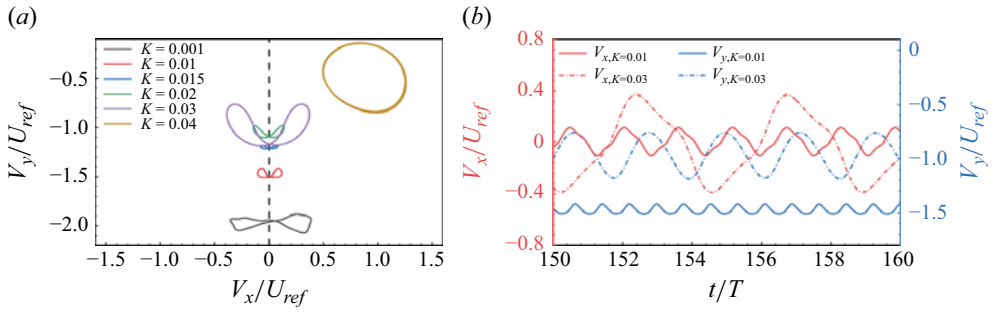


Figure 10. (*a*) Velocity limit cycles of the falling plate for different K. (*b*) Normalised horizontal velocity V_x and vertical velocity V_y as functions of time for various K. In all cases, $G = 2$.

results in symmetric periodic swinging, with alternating flapping of the arms. The wake structure (figure 9*a*) exhibits two co-rotating vortex pairs per cycle, indicating nonlinear coupling between the flapping motion and lateral oscillations.

(ii) Stable falling: as K increases, the plate forms a stable 'U' shape with approximately symmetric pressure distribution (figure 8*a*ii), where f_n is symmetrically distributed (figure 8*a*iv). This mode functions like a parachute, with stable fluid drag balancing concentrated weight, maintaining a vertical descent. This stable translation is further confirmed by the predominantly downward velocity vectors in figure 8(*IId*). Correspondingly, the fluid torque (figure 8*c*ii) exhibits only minimal, small-amplitude fluctuations, reflecting the highly stabilised attitude. The wake vorticity (figure 9*b*) shows alternating single vortices, sustaining the symmetric pressure field.

(iii) Fluttering: the plate follows a zigzag trajectory with significant lateral drift. A stronger low-pressure zone develops at the flatter end (figure 8*a*iii), amplifying the normal force (figure 8*diii*) and suppressing tumbling. As shown in figure 8(*c*iii), this asymmetric force distribution generates large-amplitude, periodic torque oscillations that alternate about zero, effectively reversing the plate's rotation (as highlighted by the velocity vectors). This mechanism provides a strong vertical fluid force and a restoring moment, driving the plate into the fluttering state, with a vortex-shedding pattern shown in figure 9(*c*).

(iv) Tumbling: the plate rotates continuously, creating a high-pressure zone on one side and a low-pressure zone on the opposite side (figure 8*aiv*). This asymmetric pressure distribution produces a periodically varying hydrodynamic torque, as shown in figure 8(*civ*). The phase relationship between the hydrodynamic torque and the rotational motion determines the hydrodynamic work done on the plate over a tumbling cycle. The continuous unidirectional rotation is evident from the velocity vectors in figure 8(*d*iv). The wake vorticity (figure 9*d*) shows a tilted vortex street, leading to continuous lateral drift.

To visualise the descent dynamics, we project the velocity trajectories of the plate's centre onto the V_xV_y phase plane. The limit cycles for varying K at a fixed concentrated weight $G = 2$ are shown in figure 10(*a*). For $K = 0.001$ and $K = 0.01$, the plate exhibits the swing mode, with limit cycles resembling lemniscates, suggesting frequency locking between the horizontal and vertical velocities. As stiffness increases, the plate transitions to the stable falling and fluttering modes, with limit cycles expanding and eventually shifting away from the $V_x = 0$ axis for the tumbling mode. It is noticed that the limit

https://doi.org/10.1017/jfm.2026.11908 Published online by Cambridge University Press

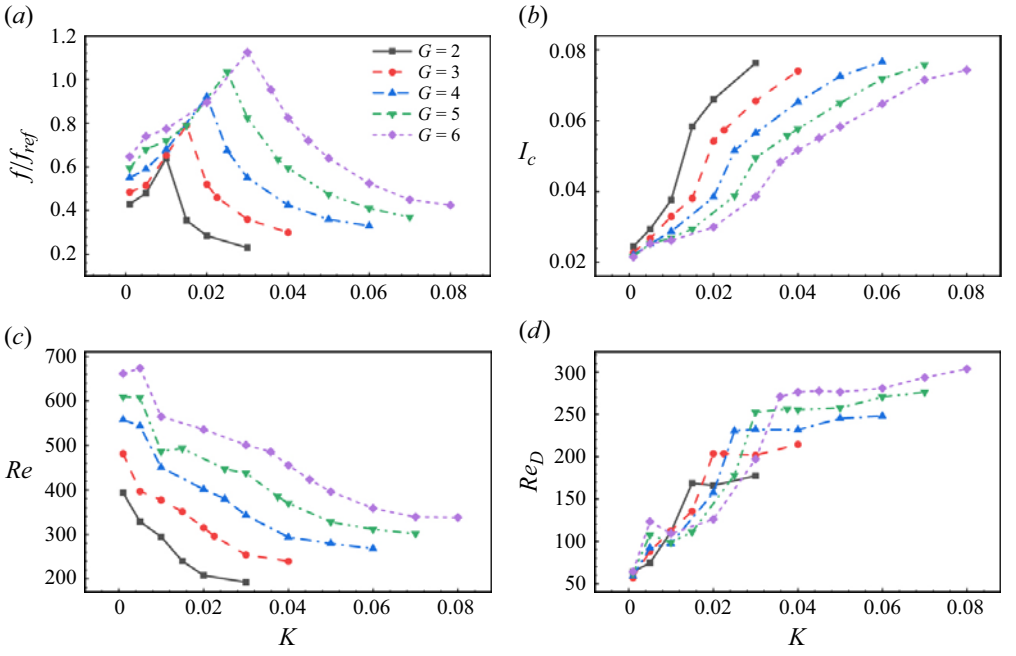


Figure 11. Normalised time-averaged (*a*) frequency f, (*b*) moment of inertia I_c, (*c*) Reynolds number Re and (*d*) distance-based Reynolds number Re_D of the falling plate as functions of K for various G. The frequency is normalised by $f_{ref} = U_{ref}/L$.

cycle for $K = 0.001$ is distorted due to large deformations at very low stiffness, where the plate's leading and trailing edges may contact during descent.

Figure 10(*b*) compares the time histories of velocity for $K = 0.01$ (swing) and $K = 0.03$ (fluttering), showing that, in both cases, the horizontal velocity V_x oscillates at half the frequency of the vertical velocity V_y, characteristic of the flutter-like motion in the swing mode.

Figure 11 summarises the trends of key physical quantities as functions of K for various G. The analysis focuses on the swing, stable falling and fluttering regimes, excluding the tumbling mode due to its distinct dynamics. Figure 11(*a*) shows the variation of normalised frequency f/f_{ref} with stiffness. Here, f is defined as the dominant frequency of the lateral force $F_x(t)$ acting on the plate during the steady descent stage, extracted from the primary peak of its power spectrum. As K increases, f rises, peaks near the swing–stable falling transition, and decreases in the stable falling regime, reflecting the plate's deformation and oscillation characteristics. Upon entering the fluttering regime, f plateaus.

At extremely low stiffness, the plate is prone to excessive folding, where the lateral reciprocating motion is constrained by the geometric configuration and the effective FSI length. As K increases, the plate adopts a more extended configuration, allowing for more effective flapping of the ends, thereby enhancing the lateral response frequency. Additionally, as G increases, the entire frequency curve shifts towards higher K values, indicating that a larger concentrated weight requires higher stiffness to trigger the same sequence of mode transitions.

Figure 11(*b*) plots the moment of inertia relative to the centre of mass, $I_c = \sum m_i r_i^2$, where m_i and r_i denote the nodal mass and its distance from the centre of mass,

https://doi.org/10.1017/jfm.2026.11908 Published online by Cambridge University Press

respectively. It is seen that I_c increases with K, reflecting the plate's extension as it transitions from a curled state to a more extended configuration. For a given K, a larger G leads to a smaller I_c, indicating tighter folding in the plate.

Figures 11(*c*) and 11(*d*) compare Reynolds numbers based on the fixed plate length L and the time-averaged end-to-end distance D (shown in figure 1*a*) over one period. As K increases, Re decreases because the swing mode's folded streamlined profile reduces drag (at lower K), while the fluttering mode's unfolded plate increases frontal area and drag (at higher K). A larger G increases Re, indicating higher descent speed. The distance-based Reynolds number Re_D initially increases with K because the growth of D outweighs the reduction in descent speed U_d. Eventually, Re_D plateaus as the growth of D slows and balances the decrease in U_d, leading to a stable configuration.

4.1.2. *Rescaling*

In figure 11, physical quantities show similar trends for different G, but do not collapse onto a single curve when plotted against K. The phase diagram in figure 7 reveals that the boundaries between the modes lie along lines where $K \propto G$, suggesting that the ratio K/G serves as the intrinsic control parameter. Physically, the system involves three characteristic forces: the elastic force (γ/L^2), the fluid force ($\rho U^2 L$) and the concentrated weight (G_c). Since the fluid force balances the weight in the terminal descent, the system's dynamics effectively reduces to a competition between the elastic restoring force and the gravitational force. When K/G is small (weak stiffness or strong weight), the plate curls; as the ratio increases, the plate unfurls, transitioning into stable falling and fluttering regimes. Geometric quantities like moment of inertia I_c and average end-to-end distance D are governed by this ratio. Thus, we define the dimensionless parameter, effective stiffness Kg, as

$$Kg = \frac{\gamma}{2G_c L^2} = \frac{K}{G}. \tag{4.5}$$

To unify the scaling of kinematics, we derive the characteristic velocity scale based on the balance between the concentrated weight and fluid drag. The fluid dynamic force scales as $F_D \sim \rho U_d^2 L$, while the gravitational force is proportional to G_c. Substituting $G_c = G\ F_{ref} = G((1/2)\rho U_{ref}^2 L)$ into the force balance, we get

$$\rho U_d^2 L \sim G\left(\frac{1}{2}\rho U_{ref}^2 L\right). \tag{4.6}$$

This yields

$$Re \sim \sqrt{G}. \tag{4.7}$$

To validate this scaling law, figure 12 plots Re versus G for three representative values of Kg. As shown, both the numerical results and fitted curves exhibit square-root scaling, with distinct intercepts for different Kg values. Here, we define a gravitational velocity $U_g = U_{ref}\sqrt{G}$. The above result indicates that U_g is a more appropriate characteristic velocity than U_{ref} for this problem.

Therefore, we substitute U_{ref} with U_g to re-nondimensionalise these physical quantities

$$f^* = \frac{fL}{U_g},\ Re^* = \frac{ReU_{ref}}{U_g},\ Re_D^* = \frac{Re_D U_{ref}}{U_g}. \tag{4.8}$$

https://doi.org/10.1017/jfm.2026.11908 Published online by Cambridge University Press

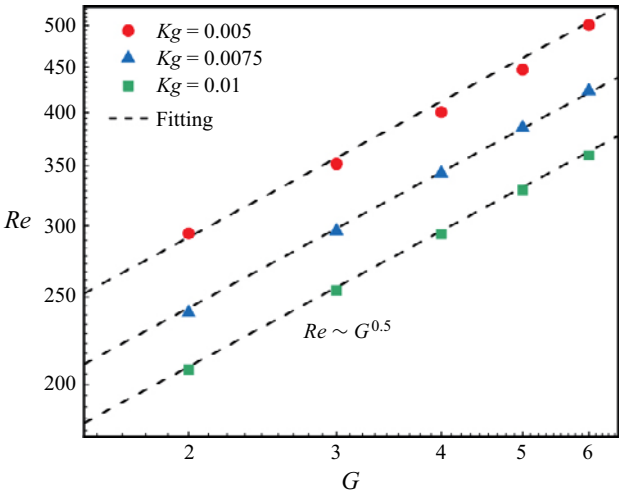


Figure 12. The Reynolds number Re as a function of concentrated weight G for various Kg. The dotted lines are the fitted curves.

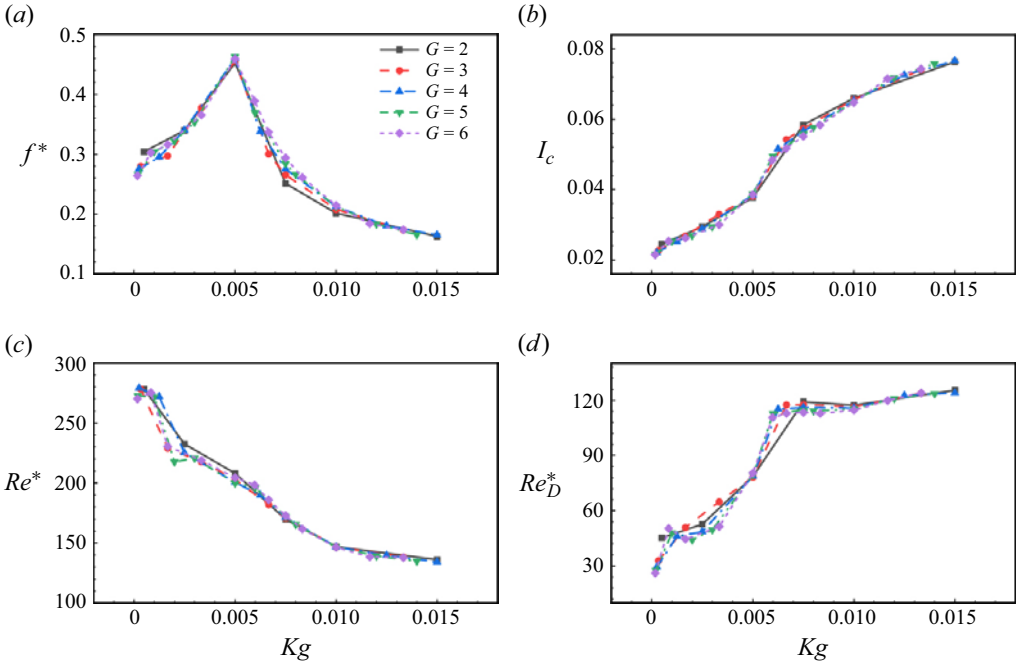


Figure 13. (a) The scaled frequency f^*, (b) moment of inertia I_c, (c) rescaled Reynolds number Re^* and (d) rescaled distance-based Reynolds number Re^*_D of the falling plate as functions of Kg for various G.

The rescaled results, shown in figure 13, collapse onto a single master curve when plotted against Kg. Specifically: (i) f^* increases and then decreases with Kg, peaking near the swing-to-stable transition (figure 13a); (ii) I_c increases monotonically with Kg (figure 13b), confirming that the geometric state (curled in swing mode or extended in fluttering) depends solely on the relative magnitudes of elastic and gravitational forces;

https://doi.org/10.1017/jfm.2026.11908 Published online by Cambridge University Press

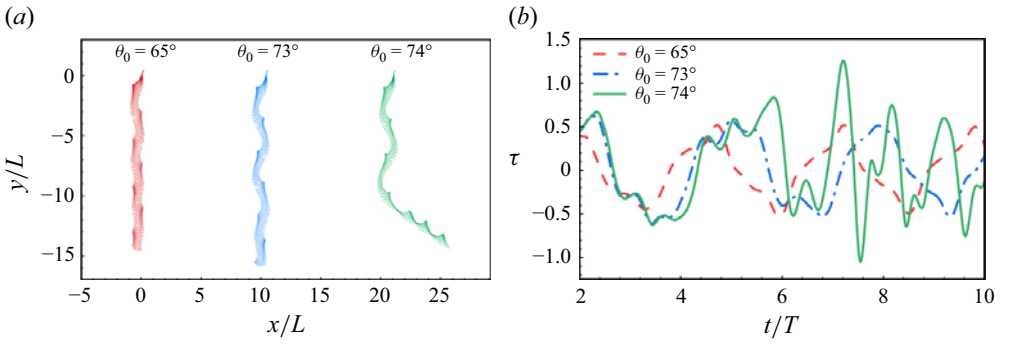


Figure 14. Evolution of the falling plate at $G = 5$ and $Kg = 0.014$ for various initial inclination angles θ_0: (a) trajectories and instantaneous shape evolution; (b) time histories of the normalised fluid torque τ evaluated with respect to the centre of mass.

(iii) Re^* decreases (figure 13c), while Re^*_D increases and plateaus (figure 13d). This consistent collapse confirms that Kg is an effective control parameter.

4.1.3. *Bistability and critical transition angle*

We focus on the bistable region (green area in figure 7), where the final steady state depends on the initial inclination angle θ_0, as shown by the transition between fluttering and tumbling modes. This bistability, similar to the findings of Lau *et al.* (2018) for rigid plates, arises from two competing basins of attraction in phase space: the plate settles into the fluttering state for $\theta_0 < \theta_{cr}$ and into the tumbling state for $\theta_0 > \theta_{cr}$. Extensive simulations confirm that in the swing, stable falling and high-stiffness tumbling regimes, the plate's motion always converges to a unique limit cycle, regardless of θ_0.

To understand the transition from fluttering to tumbling, figure 14 shows the effect of θ_0 on the descent dynamics for fixed parameters ($G = 5$, $Kg = 0.014$). For $\theta_0 = 65°$, the plate settles into a stable fluttering state. At $\theta_0 = 73°$, the plate exhibits larger initial lateral excursions but eventually settles into fluttering after fluid damping dissipates excess energy. At $\theta_0 = 74°$, the plate transitions abruptly to the tumbling state after reaching a critical turning point.

The normalised fluid torque history evaluated with respect to the centre of mass (figure 14b) physically elucidates this bifurcation. For cases settling into fluttering ($\theta_0 = 65°$ and $73°$), the initial torque oscillations gradually damp out, recovering a symmetric, reciprocal balance that sustains the zigzag trajectory. Conversely, at the critical angle $\theta_0 = 74°$, a strong unidirectional destabilising torque peak emerges at the first turning point ($t/T \approx 7$). This peak breaks the reciprocal balance and imparts sustained angular momentum, triggering the continuous rotation of the tumbling mode.

With the mechanism clarified, we examine the critical threshold. Figure 15(a) shows θ_{cr} decreases monotonically with increasing K, meaning stiffer plates are more prone to tumbling with smaller initial perturbations. Higher stiffness maintains a large angle of attack and flow asymmetry, which generates a net torque to sustain continuous rotation. Conversely, flexible plates (K smaller) need a larger initial inclination to overcome restoring forces and reach the tumbling regime. As G increases, the entire curve shifts towards higher K, indicating that a stronger concentrated weight requires higher K to trigger the mode switch.

Figure 15(b) shows that θ_{cr} curves collapse onto a single line when plotted against effective stiffness Kg, confirming that bistability is governed by the ratio of structural

https://doi.org/10.1017/jfm.2026.11908 Published online by Cambridge University Press

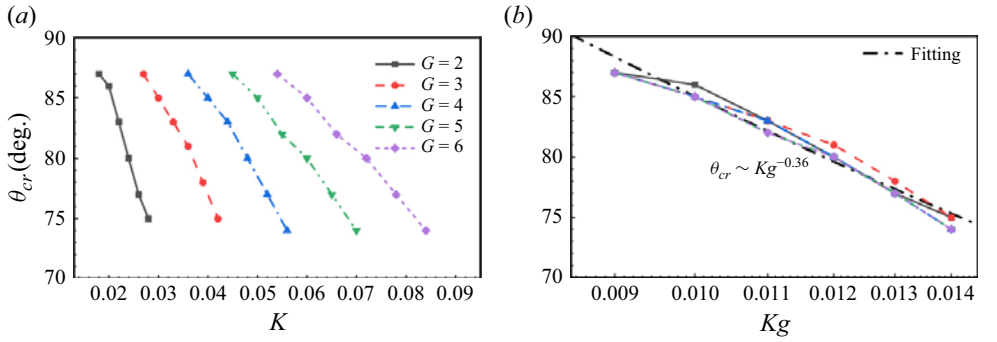


Figure 15. Critical inclination angle θ_{cr} of the falling plate as a function of: (*a*) K and (*b*) Kg for various G.

stiffness to gravitational driving force. This result extends the power-law relationship between I_c and Re for rigid plates, established by Lau *et al.* (2018), to flexible systems. The critical transition angle follows a power-law relationship

$$\theta_{cr} \approx 16.2 Kg^{-0.36}. \tag{4.9}$$

This formula quantifies the decay of θ_{cr} with Kg, indicating that, for a given Kg, the threshold for triggering tumbling is constant, regardless of the gravitational load.

4.1.4. *Transition of vortex-shedding modes in the swing regime*

In the previous section, we discussed the bistable nature of the fluttering–tumbling transition, which is influenced by θ_0. Further analysis reveals that even within a single motion mode, the wake's topological structure can change as control parameters vary. This is especially noticeable in the swing mode: as the mass ratio M decreases, the vortex-shedding pattern transitions from a 2P mode to a 2S mode.

Figure 16 shows the instantaneous spanwise vorticity ω_z for the swing mode at fixed parameters ($G = 4$, $Kg = 0.003$) and different mass ratios M. At $M = 0.8$, the wake exhibits a typical 2P mode, with two pairs of vortices shed per oscillation cycle. As M decreases to 0.7, the flow simplifies, transitioning to a 2S mode, where only a single pair of alternating vortices is shed per cycle, forming a stable Kármán vortex street.

This topological transition in the wake is tightly coupled with the dynamic structural loading. Figure 17 plots the time histories of the normalised fluid torque T_z for $M = 0.7$ and $M = 0.8$ at the same physical parameters. In the 2S regime ($M = 0.7$), the fluid torque exhibits a relatively simple, smooth periodic waveform, which directly corresponds to the regular alternating vortex shedding. Conversely, upon entering the 2P regime ($M = 0.8$), the torque evolution becomes highly complex, manifesting as a distinct multi-peak signature within each oscillation cycle. This multi-peak behaviour serves as direct mechanical evidence of the secondary vortex formation and split-shedding processes inherent to the 2P wake structure.

This transition from 2P to 2S is unique to the swing mode. In contrast, the stable falling, fluttering and tumbling modes consistently maintain a 2S wake structure, regardless of M. This section focuses on the mechanism behind this transition and establishes a physical criterion for the mode boundary.

To explore the shedding mode transition, we scanned the (G, M) parameter space for $Kg < 0.005$ (swing regime), as shown in figure 18. The phase diagram clearly shows that the 2S mode dominates at low G and M, while the 2P mode occupies higher G and M

https://doi.org/10.1017/jfm.2026.11908 Published online by Cambridge University Press

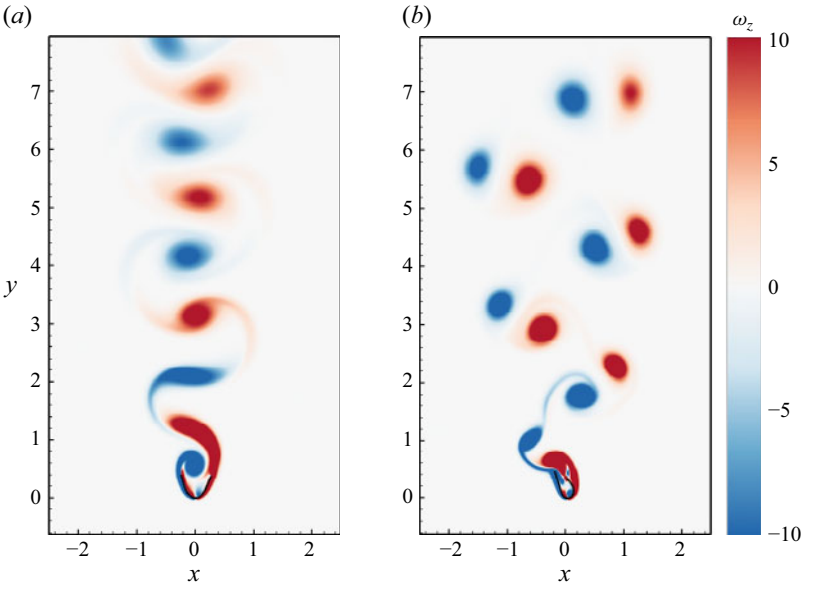


Figure 16. Instantaneous vorticity contours around the falling plate at $G = 4$ and $Kg = 0.003$: (a) mass ratio $M = 0.7$; (b) mass ratio $M = 0.8$.

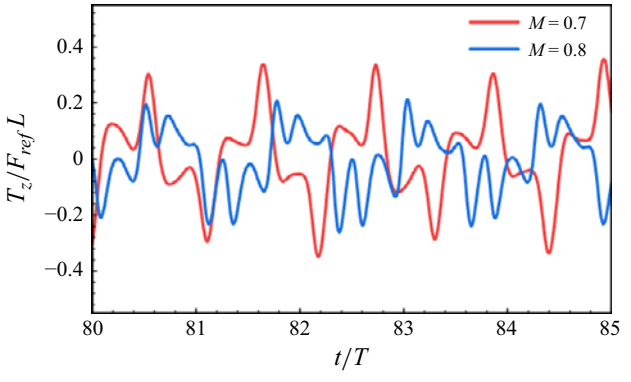


Figure 17. Time histories of the normalised hydrodynamic torque T_z evaluated with respect to the centre of mass for the swing mode at fixed parameters $G = 4$ and $Kg = 0.003$ under different mass ratios: $M = 0.7$ and $M = 0.8$.

regions. The critical mass ratio M_{cr} defines the boundary for the 2S mode; for $M > M_{cr}$, the system transitions to the 2P regime.

At a fixed Kg, the critical mass ratio decreases with increasing G. For example, at $Kg = 0.002$, the 2S mode persists up to $M = 0.5$ at $G = 2$, but shifts to $M = 0.4$ at $G = 3$ and to $M = 0.2$ at $G = 6$. This suggests that higher weight increases wake instability, making vortex pair splitting easier.

As Kg increases, the stable region for the 2S mode expands, as shown in the comparison of different Kg values. This indicates that larger stiffness and smaller mass ratios suppress vortex splitting, favouring the 2S mode.

To clarify the shedding mode transition, we analyse the plate's motion time scales across the transition boundary ($Kg = 0.003$, $G = 4$). The oscillation period T_f, driven by plate

https://doi.org/10.1017/jfm.2026.11908 Published online by Cambridge University Press

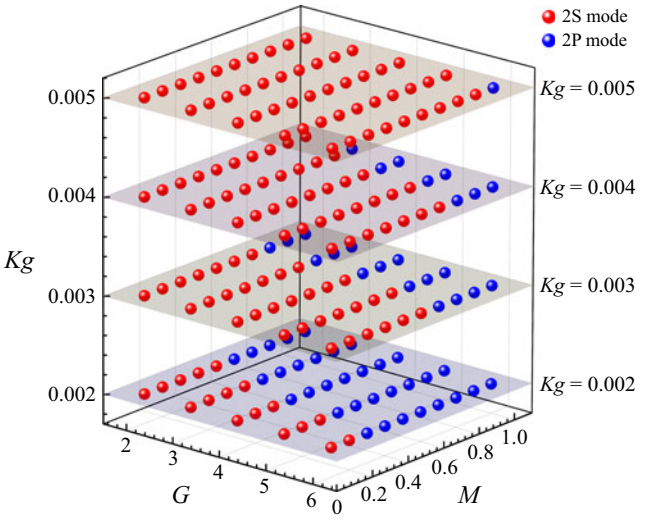


Figure 18. Three-dimensional phase diagram of vortex-shedding modes in the (G, M, Kg) parameter space. Red spheres represent the 2S mode, while blue spheres denote the 2P mode. Semi-transparent horizontal planes show cross-sections at fixed effective stiffness $Kg = 0.002, 0.003, 0.004, 0.005$.

flapping, is key to vortex shedding. Analysis shows the period elongates as the system moves from 2S to 2P. For $M = 0.7$ (2S), the period is $T_f/T_{ref} \approx 1.10$, while for $M = 0.8$ (2P), it increases to $T_f/T_{ref} \approx 1.266$. This longer period in 2P allows more time for vortex formation and corresponds to a lower frequency, while the shorter period in 2S leads to faster vortex shedding.

We quantify these frequency properties using the Strouhal number

$$St = fL/U_d. \tag{4.10}$$

Figure 19 shows that St decreases monotonically with increasing M and collapses onto a single curve for different G, indicating a universal scaling law. In the 2P regime, the data follow

$$St \sim M^{-0.5}. \tag{4.11}$$

This scaling law can be derived from the force balance on the plate (Huang & Sung 2010). When the plate mass is large, the system is inertia dominated. The characteristic inertial force and fluid force can be estimated as: $F_{inertia} \sim \rho_s h L f^2 A$ and $F_{fluid} \sim \rho U_d^2 A$, respectively, where A is the lateral oscillation amplitude. Balancing these terms, $F_{inertia} \sim F_{fluid}$, i.e.

$$\rho_s h L f^2 A \sim \rho U_d^2 A, \tag{4.12}$$

yields

$$f \sim \sqrt{\rho U_d^2/(\rho_s h L)}. \tag{4.13}$$

Substituting this into the definition of St

$$St = \frac{fL}{U_d} \sim \frac{L}{U_d}\sqrt{\frac{\rho U_d^2}{\rho_s h L}} = \sqrt{\frac{\rho L}{\rho_s h}} = \sqrt{\frac{1}{M}} = M^{-0.5}. \tag{4.14}$$

https://doi.org/10.1017/jfm.2026.11908 Published online by Cambridge University Press

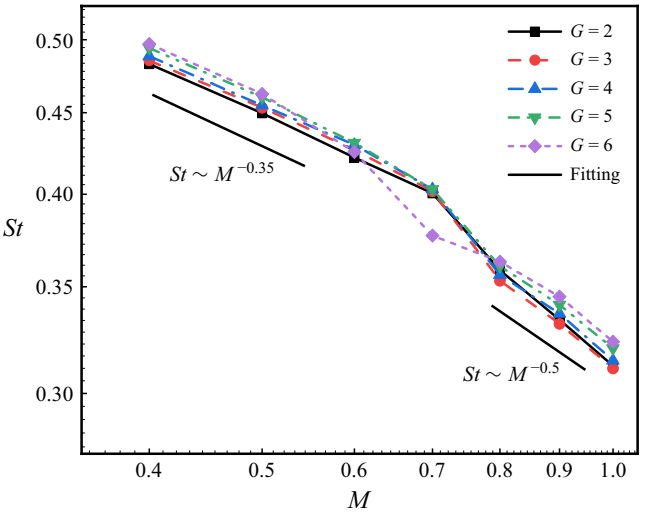


Figure 19. Strouhal number St as a function of M for various G. In all cases, $Kg = 0.003$.

In the 2S regime, the system departs from inertia-dominated behaviour characteristic of the 2P mode. In this regime, the plate oscillates at higher frequencies (larger St) with lower mass ratios, making the added mass effect non-negligible. Consequently, the effective inertial mass must account for both the structural mass and the added fluid mass, modifying the force balance in (4.12) to

$$\left(\rho_s hL + C_m \rho L^2\right) f^2 A \sim \rho U_d^2 A, \tag{4.15}$$

where C_m represents the added mass coefficient. Substituting this into the definition of the Strouhal number yields a modified scaling law

$$St = \frac{fL}{U_d} \sim \sqrt{\frac{\rho L^2}{\rho_s hL + C_m \rho L^2}} = \sqrt{\frac{1}{M + C_m}} = (M + C_m)^{-0.5}. \tag{4.16}$$

The effective scaling exponent n (the slope in the log–log plot) can be derived as

$$n = \frac{\mathrm{d} \ln St}{\mathrm{d} \ln M} = -0.5 \frac{M}{M + C_m}. \tag{4.17}$$

Since C_m is positive, the magnitude of the slope $|n|$ is strictly less than 0.5. This theoretical correction explains the shallower scaling observed in our simulations, which is best fitted by

$$St \sim M^{-0.35}. \tag{4.18}$$

The critical Reynolds number Re^*_{cr} for the wake transition from 2S to 2P is shown in figure 20. As Kg increases, Re^*_{cr} decreases, following a power-law relationship

$$Re^*_{cr} \sim Kg^{-0.28}. \tag{4.19}$$

This provides a predictive model for the critical flow conditions for the 2S-to-2P transition, governed by Kg.

Before proceeding to the 3-D results, it is instructive to clarify the distinct physical roles of the effective stiffness Kg and the dimensionless moment of inertia I^* in the present system. Following Lau & Huang (2021), the dimensionless moment of inertia is defined as

https://doi.org/10.1017/jfm.2026.11908 Published online by Cambridge University Press

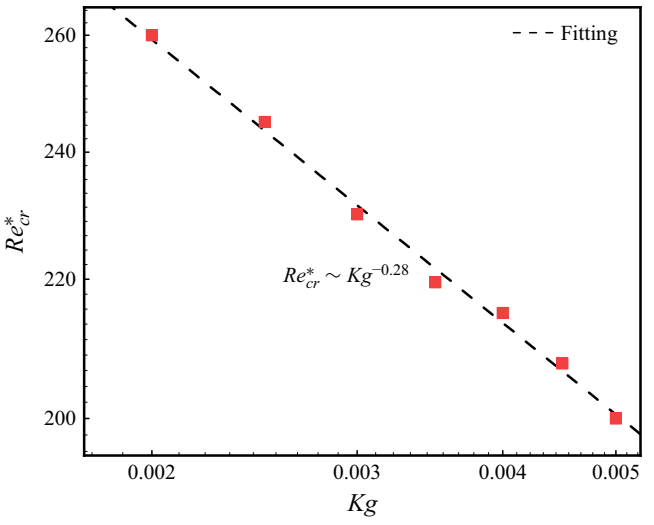


Figure 20. The critical rescaled Reynolds number Re^*_{cr} as a function of Kg. The dotted line is the fitted curve.

$I^* = 8\rho h^*(1 + h^*)/3\pi$. Given the mass ratio definition $M = \rho^* h^*$ and the assumption of thin plates ($h^* \ll 1$), this relation simplifies to $I^* \approx 8M/(3\pi)$. Consequently, in the present configuration, modulating I^* is essentially equivalent to varying the plate's mass ratio M. While Kg fundamentally governs the global stiffness-to-weight balance and dictates the primary macroscopic mode transitions (e.g. from swing to stable falling and fluttering), I^* characterises the inertial properties related to mass distribution. As demonstrated by the 2S-to-2P transition, I^* (and thus M) primarily influences the detailed wake topology and secondary vortex dynamics within a specific falling regime, rather than altering the global kinematic mode boundaries.

4.2. *Three-dimensional cases study*

Natural flyers, such as falling leaves, and artificial vehicles typically have finite wingspans. While the 2-D model provides insights into the basic dynamics, it neglects spanwise flow effects. To explore 3-D effects, we performed simulations with flexible plates of finite aspect ratios ($A_r = 0.125$, 0.25, 0.5 and 1.0) at fixed $G = 4$.

4.2.1. *Three-dimensional falling modes*

Figure 21 shows the four falling modes of a flexible plate with finite aspect ratios, consistent with the 2-D cases. The first three modes are from the $A_r = 0.25$ and $G = 4$ case. Projections from different perspectives reveal that the plate's motion and deformation are mainly confined to the initial release plane (xz-plane), characterised by planar flapping and bending, with minimal spanwise deformation. This indicates that the finite aspect ratio does not significantly affect the kinematic behaviour of these modes.

Though 2-D simulations show that high-stiffness plates easily transition to the tumbling mode, this was not observed for small aspect ratios ($A_r \leqslant 0.5$) in 3-D simulations, even at high stiffness. This is due to significant pressure leakage from the finite span, which diminishes the pressure differential between the plate's upper and lower surfaces, preventing sufficient aerodynamic forces for sustained tumbling. The tumbling mode in figure 21 was observed only for a higher aspect ratio ($A_r = 1$, $K = 1$).

https://doi.org/10.1017/jfm.2026.11908 Published online by Cambridge University Press

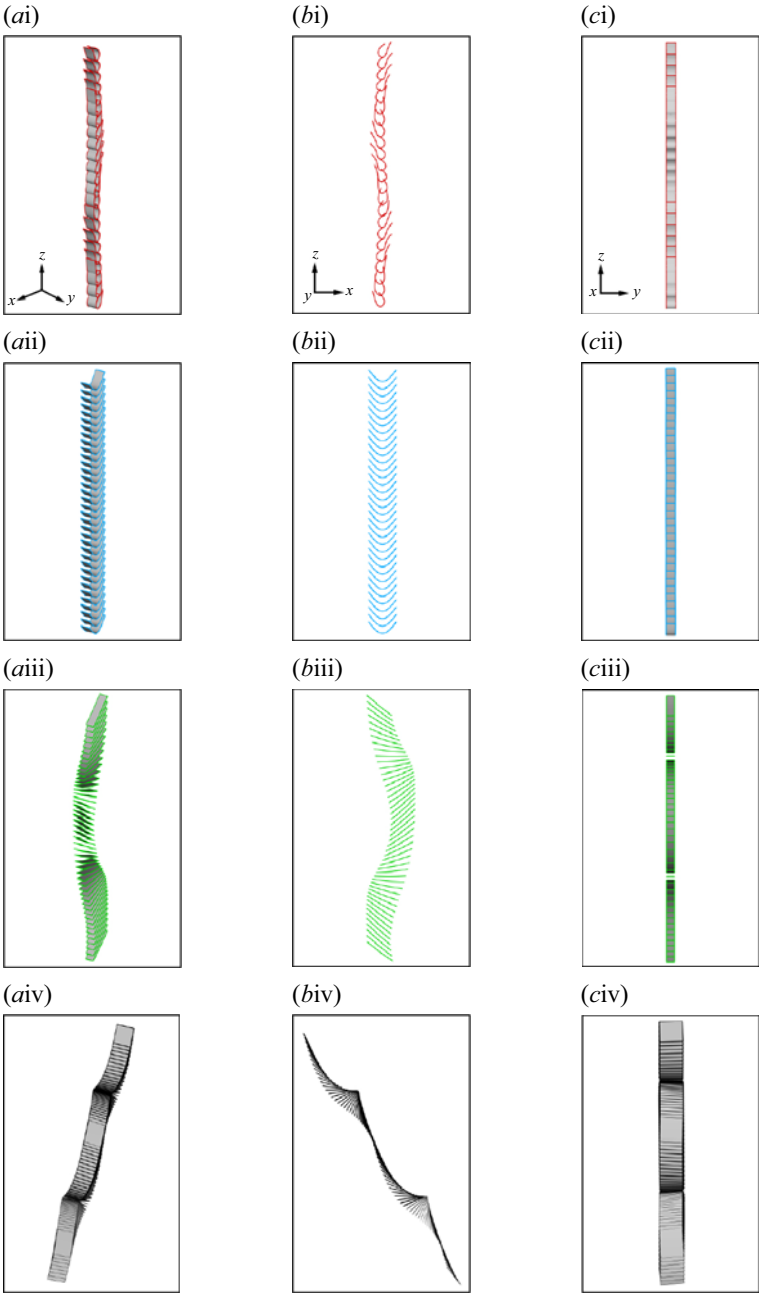


Figure 21. Visualisation of the plate exhibiting four distinct falling modes in 3-D simulations. The rows from top to bottom correspond to: (i) swing mode ($Ar = 0.25$, $K = 0.005$); (ii) stable falling mode ($Ar = 0.25$, $K = 0.03$); (iii) fluttering mode ($Ar = 0.25$, $K = 0.1$); and (iv) tumbling mode ($Ar = 1.0$, $K = 1.0$). For each mode, three perspectives are presented: column (a) the 3-D perspective view; column (b) side view of xz-plane; and column (c) side view of yz-plane. All cases are simulated at $G = 4$.

https://doi.org/10.1017/jfm.2026.11908 Published online by Cambridge University Press

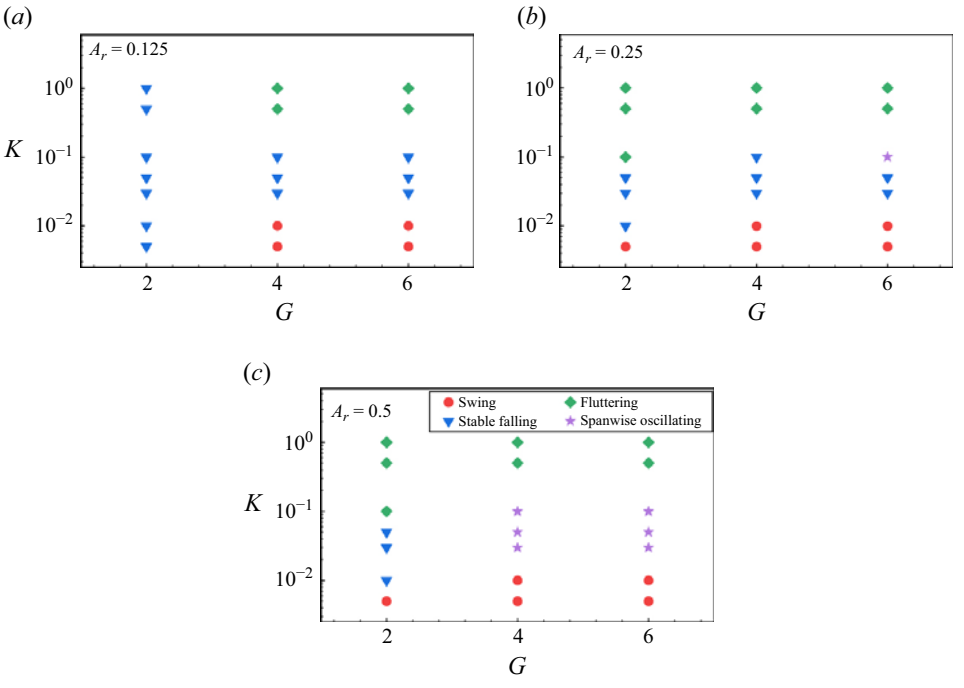


Figure 22. Phase diagrams of the 3-D falling modes in the (G, K) parameter space for flexible plates with finite aspect ratios: (*a*) $A_r = 0.125$, (*b*) $A_r = 0.25$ and (*c*) $A_r = 0.5$. Distinct symbols denote the observed descent states: swing (red circles), stable falling (blue downward triangles), fluttering (green diamonds) and the spanwise oscillating mode (purple stars).

To provide a comprehensive and quantitative counterpart to the 2-D results, figure 22 presents the regime maps of the 3-D falling modes in the (G, K) parameter space for $A_r = 0.125$, 0.25 and 0.5. For the narrowest plate ($A_r = 0.125$), strong spanwise pressure leakage effectively suppresses lateral oscillations, significantly expanding the stable falling regime into regions where fluttering typically occurs in two dimensions. As A_r increases, this leakage weakens, and the regime boundaries progressively approach the 2-D limits. Notably, at $A_r = 0.5$, a distinct 'spanwise oscillating mode' emerges in the transitional region. This mode features periodic lateral oscillations of the spanwise edges driven by 3-D side-edge vortex shedding; a detailed mechanistic analysis of this behaviour is deferred to 4.2.2.

Figure 23 shows the Reynolds-number Re variation for $A_r = 0.25$. As in the 2-D case, Re decreases with increasing K, first dropping and then plateauing. This is due to reduced effective frontal area at low stiffness, leading to lower fluid drag. As stiffness increases, the plate 'unfurls' and enters the fluttering state, where drag increases, and the descent velocity stabilises.

We also examine the applicability of the dimensionless parameter Kg for 3-D cases. After rescaling with Kg, the data collapse onto a single curve, confirming that Kg remains the key parameter governing the descent dynamics, even in 3-D flows. This collapse was observed for all aspect ratios ($A_r = 0.125$, 0.25, 0.5). For clarity, only the result for $Ar = 0.25$ is shown.

https://doi.org/10.1017/jfm.2026.11908 Published online by Cambridge University Press

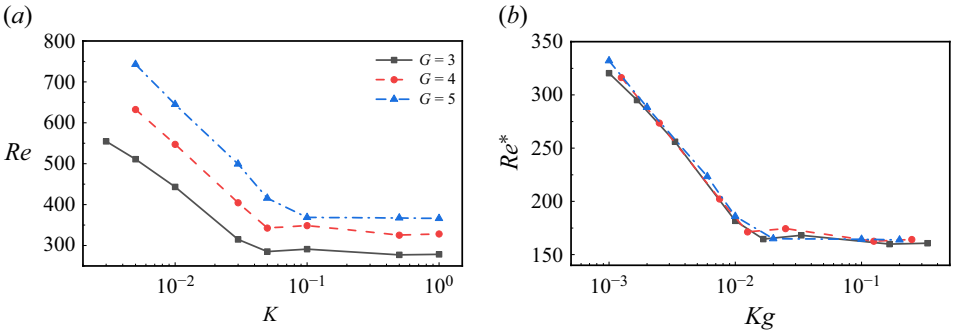


Figure 23. Time-averaged Reynolds number for $A_r = 0.25$: (*a*) Re as a function of K for various G. (*b*) Rescaled Reynolds number Re^* plotted against Kg for the same cases.

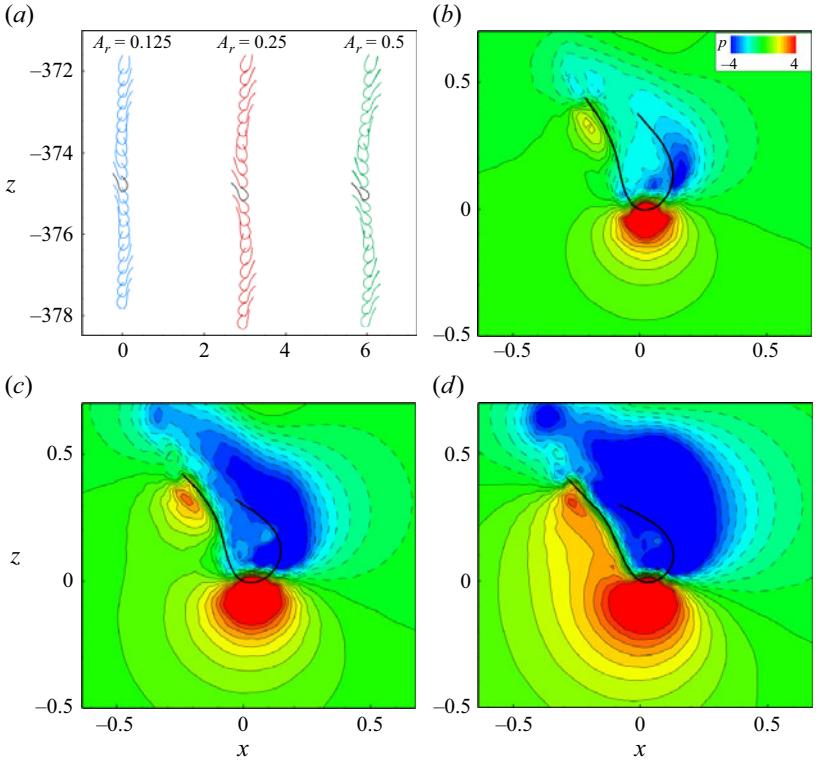


Figure 24. Comparison of the swing mode for plates with different aspect ratios at $G = 4$ and $K = 0.005$. (*a*) Trajectories of the plate centre projected onto the xz-plane for $Ar = 0.125$ (blue), $Ar = 0.25$ (red) and $Ar = 0.5$ (green). The instantaneous shapes at the turning point are highlighted in black. (*b–d*) Pressure contours around the plate at corresponding turning points for (*b*) $Ar = 0.125$, (*c*) $Ar = 0.25$ and (*d*) $Ar = 0.5$.

4.2.2. *Influence of aspect ratio on falling modes*

To investigate the impact of aspect ratio A_r on the descent dynamics, we fix $G = 4$ and compare the behaviour of three modes (swing, stable falling and fluttering) for $A_r = 0.125$, $A_r = 0.25$ and $A_r = 0.5$.

In the swing mode at low stiffness ($K = 0.005$), figure 24(*a*) shows that increasing A_r enhances the lateral swing amplitude and increases bending deformation. For

https://doi.org/10.1017/jfm.2026.11908 Published online by Cambridge University Press

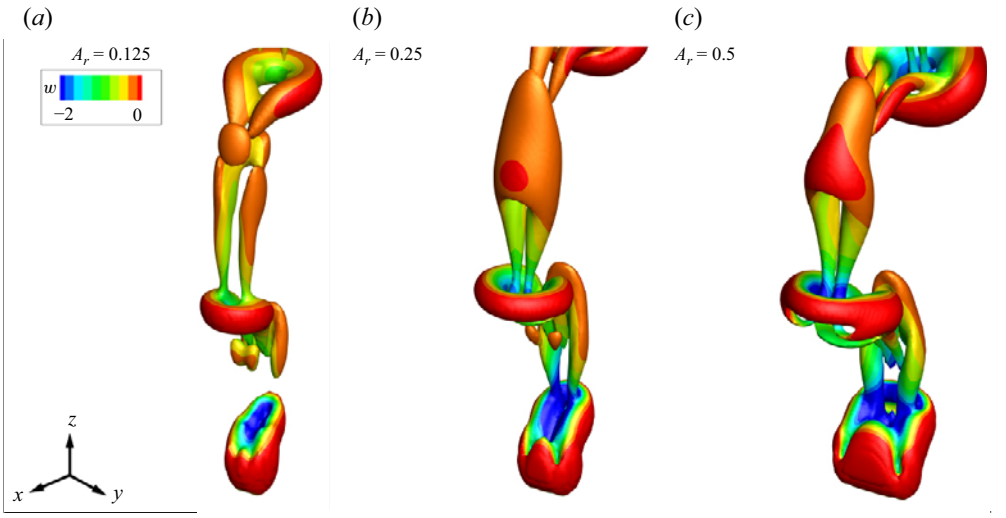


Figure 25. Instantaneous vortex structures of the swing mode visualised by iso-surfaces of the Q-criterion ($Q = 0.1$), where ($Q = (1/2)(\|\boldsymbol{\Omega}\|^2 - \|\boldsymbol{D}\|^2)$ is the second invariant of the velocity-gradient tensor, and $\boldsymbol{\Omega}$ and $\boldsymbol{D}$ denote the rotation-rate and strain-rate tensors, respectively. The iso-surfaces are coloured by the velocity in the z-direction w for (a) $A_r = 0.125$, (b) $A_r = 0.25$ and (c) $A_r = 0.5$.

$A_r = 0.5$, the plate exhibits the maximum 'U'-shaped curvature, while $A_r = 0.125$ remains relatively flat. This difference in kinematics is due to the pressure distribution, shown in figure 24(b–d). At $A_r = 0.125$, fluid leaks around the edges, leading to pressure equalisation and diminished normal force, which reduces lateral displacement and bending. As A_r increases, pressure differential is better maintained, generating stronger lateral forces and larger oscillations.

Figure 25 shows the vortex structures in the wake for each aspect ratio. At $A_r = 0.125$ (figure 25a), vortices are weak and diffuse, while at $A_r = 0.5$ (figure 25c), they become stronger and more compact, indicating enhanced vortex strength and coherence. This reflects the influence of aspect ratio on pressure differential and vortex formation. Specifically, a wider plate possesses a larger surface area, leading to a stronger interaction with the surrounding fluid and, consequently, increased vortex intensity.

Similar to the 2-D case, the mass ratio M significantly affects vortex shedding in the 3-D swing mode. Figure 26 shows the instantaneous vortex structures for two mass ratios at fixed parameters ($G = 4$, $A_r = 0.5$, $K = 0.005$). For $M = 0.5$ (figure 26a,b), the wake maintains coherent vortex loops, preserving a clean topological structure. However, at $M = 1.0$ (figure 26c,d), the wake becomes more fragmented, with primary vortices breaking into smaller, scattered vortices. This fragmentation at higher mass ratios, similar to the transition from 2S to 2P shedding in 2-D simulations, highlights the destabilising effect of mass ratio on wake topology, which persists in 3-D flows.

At intermediate stiffness ($K = 0.03$), for $A_r = 0.5$, a new mode, the spanwise oscillating mode, emerges. In figure 27, the top view shows that the two short edges of the plate remain stationary, while the long edges undergo periodic lateral oscillations. This motion suggests a Hopf bifurcation, where the oscillation induced by tip/side-edge flows is superimposed on the stable descent.

Figure 28 shows the Q-criterion iso-surfaces for the spanwise oscillating mode. For smaller aspect ratios ($A_r = 0.125$ and 0.25), the vortices are weak and localised. However,

https://doi.org/10.1017/jfm.2026.11908 Published online by Cambridge University Press

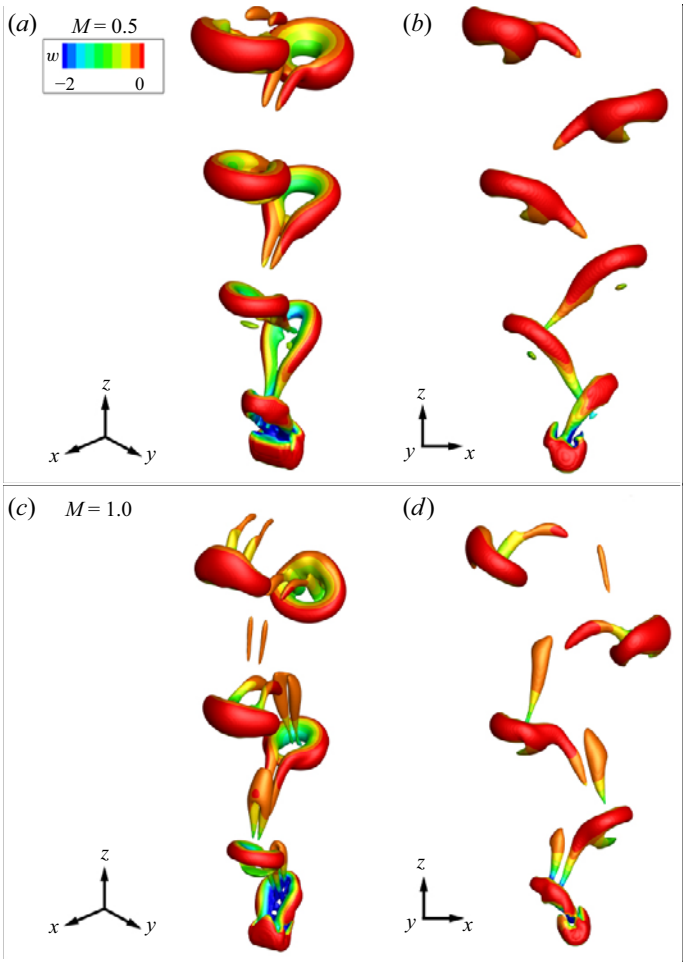


Figure 26. Instantaneous vortex structures of the swing mode visualised by iso-surfaces of the Q-criterion ($Q = 0.1$) coloured by the velocity in the z-direction w for (a–b) $M = 0.5$ and (c–d) $M = 1.0$. In all cases, $G = 4$, $Ar = 0.5$.

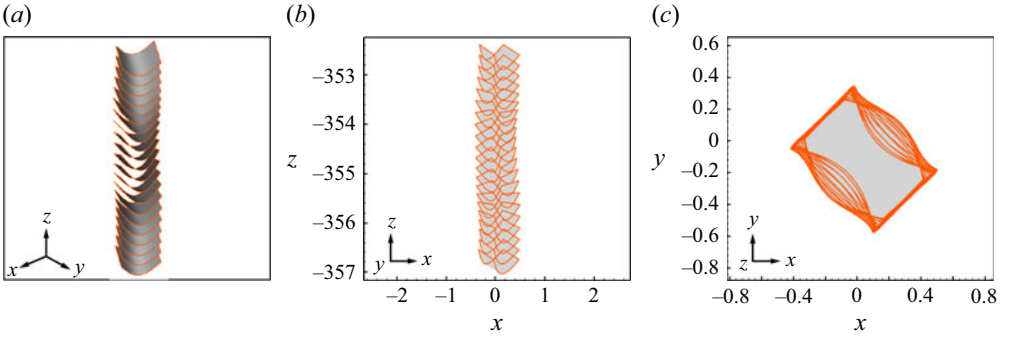


Figure 27. The spanwise oscillating mode observed at $Ar = 0.5$ ($K = 0.03$, $G = 4$). (a) Three-dimensional perspective, (b) side view in the xz-plane and (c) top view in the xy-plane.

https://doi.org/10.1017/jfm.2026.11908 Published online by Cambridge University Press

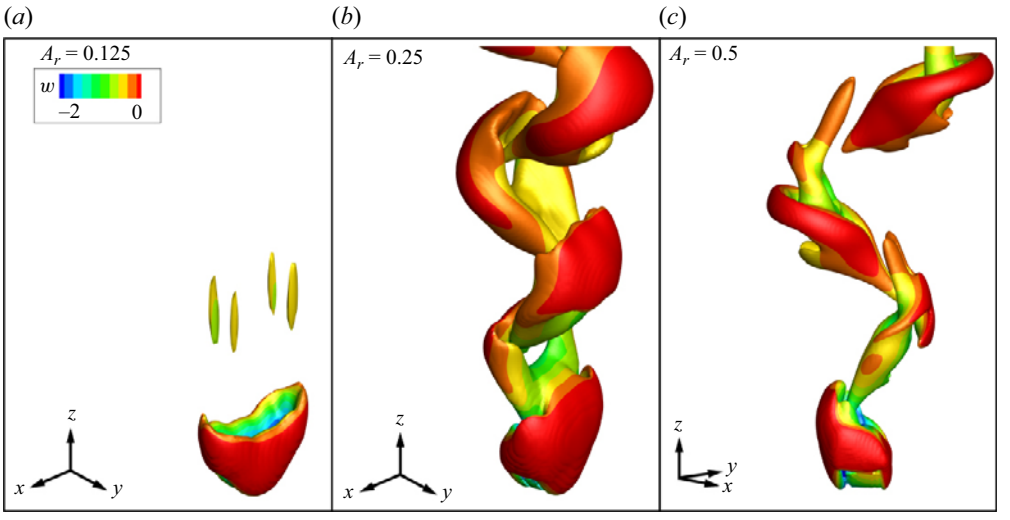


Figure 28. Instantaneous 3-D vortex structures visualised by iso-surfaces of the Q-criterion ($Q = 0.1$) coloured by the velocity in the z-direction w for (a) $Ar = 0.125$, (b) $Ar = 0.25$ and (c) $Ar = 0.5$. In all cases, $K = 0.03$, $G = 4$.

at $A_r = 0.5$, the vortices become more intense and shed periodically, generating stronger lateral forces and inducing oscillations. This effect is attributed to the larger aspect ratio facilitating a more stable vortex structure and stronger hydrodynamic forces.

In the fluttering mode at high stiffness ($K = 0.1$), the lateral drift amplitude increases with A_r (figure 29a). The wider plates ($A_r = 0.5$) experience more significant lateral excursions compared with narrower ones ($A_r = 0.125$). As shown in figure 29(b–d), the pressure distribution at the turning point shows stronger pressure differentials for larger A_r, leading to greater lateral driving forces and larger oscillation amplitudes.

In the fluttering mode, the vortex coherence and intensity increase with A_r. For narrower plates ($A_r = 0.125$), the vortices are weak, while for wider plates ($A_r = 0.5$), the vortex structure is stronger and more coherent, contributing to enhanced hydrodynamic forces that drive larger lateral oscillations (figure 30).

5. Concluding remarks

In this study, we conducted numerical simulations to investigate the sedimentation of a flexible plate driven by a concentrated central weight. By exploring the parameter space of bending stiffness K, concentrated weight G and mass ratio M, we examined the interplay between structural flexibility and the concentrated weight configuration.

In the 2-D simulations, we identified four distinct falling modes: swing, stable falling, fluttering and tumbling. The introduction of a concentrated weight leads to significant curvature, giving rise to the unique swing and stable falling modes in the low-stiffness regime. We identified the effective stiffness ratio $Kg = K/G$ as the key control parameter, which governs the competition between elastic restoring and gravitational forces and successfully collapses the transition boundaries and kinematic characteristics.

We also explored the nonlinear dynamics within specific regimes. A bistable region was found at the fluttering–tumbling transition, where mode selection is sensitive to the initial release angle θ_0. We established a scaling law for the critical transition angle, $\theta_{cr} \sim Kg^{-0.36}$, which quantifies the threshold for tumbling. Additionally, in the swing mode, we observed a transition in the wake from a 2P to a 2S shedding mode, driven

https://doi.org/10.1017/jfm.2026.11908 Published online by Cambridge University Press

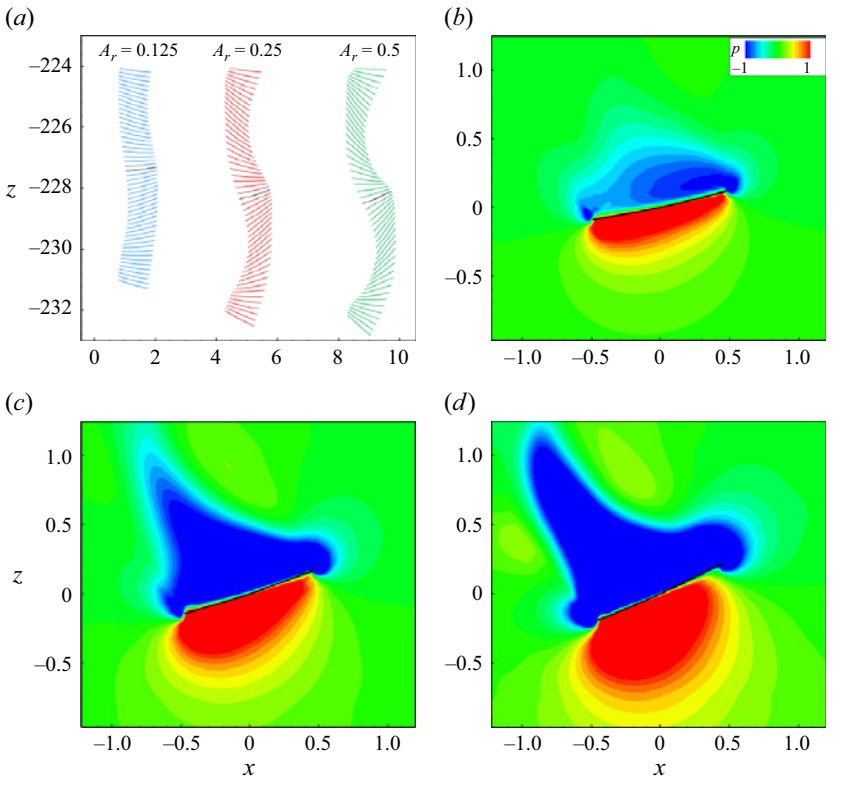


Figure 29. Comparison of the fluttering mode for plates with different aspect ratios at $G = 4$ and $K = 0.1$. (*a*) Trajectories of the plate centre projected onto the xz-plane for $Ar = 0.125$ (blue), $Ar = 0.25$ (red) and $Ar = 0.5$ (green). The instantaneous shapes at the turning point are highlighted in black. (*b–d*) Pressure contours p around the plate at the corresponding turning instants marked in (*a*) for (*b*) $Ar = 0.125$, (*c*) $Ar = 0.25$ and (*d*) $Ar = 0.5$.

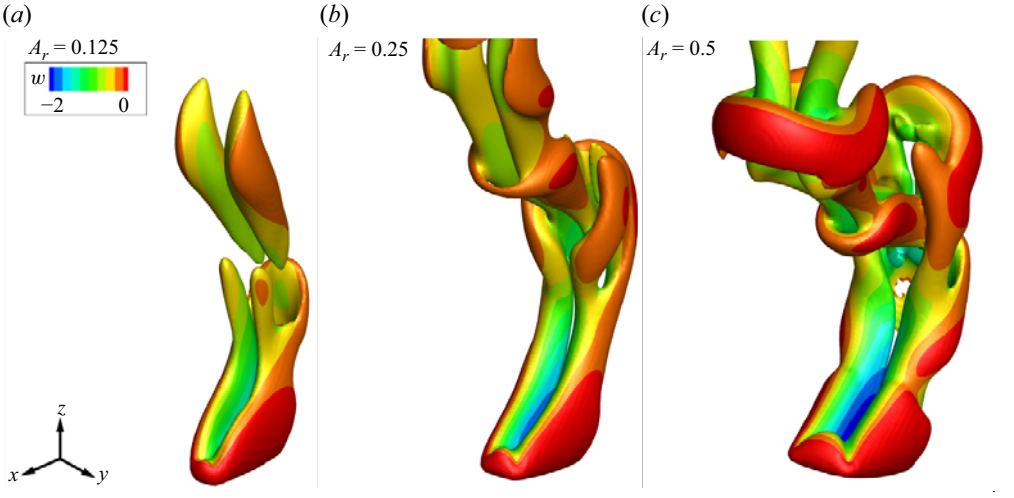


Figure 30. Instantaneous vortex structures of the fluttering mode visualised by iso-surfaces of the Q-criterion ($Q = 0.1$) coloured by the velocity in the z-direction w for (*a*) $Ar = 0.125$, (*b*) $Ar = 0.25$ and (*c*) $Ar = 0.5$ at the turning point in figure 29.

https://doi.org/10.1017/jfm.2026.11908 Published online by Cambridge University Press

by the balance between fluid inertial forces and structural response, with a critical Reynolds-number scaling $Re^*_{cr} \sim Kg^{-0.28}$.

Our 3-D simulations revealed the significant influence of the aspect ratio A_r. The Kg scaling law remains robust for finite-span plates, but pressure leakage at low A_r suppresses the aerodynamic forces required for tumbling. As A_r increases, new modes emerge, such as the spanwise oscillating mode that bifurcates from the stable falling mode.

It should be noted that the present study is limited to a laminar, unsteady separated-flow regime, with terminal Reynolds numbers approximately in the range $Re = 200-700$. Therefore, the present mode classification, wake-transition behaviour and Kg-based scaling should not be directly extrapolated to high-Reynolds-number turbulent regimes. In addition, the immersed boundary formulation used here is intended to capture the global FSI and large-scale wake dynamics, rather than the near-wall boundary layer or the exact separation location. This limitation is expected to be less critical for the stable falling, fluttering and tumbling modes, where separation is mainly edge dominated. For the swing mode, however, the strongly curved plate may allow separation to occur upstream of the geometric edge, which may introduce quantitative uncertainty in the local normal-force distribution and wake-transition threshold. Nevertheless, the verification tests, grid- and time-step-independence studies, and the consistent Kg-based collapse indicate that the main conclusions remain robust within the present parameter range.

These findings provide new insights into the passive flight of non-uniformly weighted structures in nature and offer theoretical guidance for the design and optimisation of bio-inspired micro-air vehicles.

Acknowledgements. Calculations were performed at the Supercomputing Centre of the University of Science and Technology of China.

Funding. This work was supported by the Natural Science Foundation of China (NSFC) grant nos 11972342, 11772326, 12388101, 12502308, the Postdoctoral Fellowship Program of CPSF under grant no. GZC20241645 and the China Postdoctoral Science Foundation under grant no. 2025M781800.

Declaration of interests. The authors report no conflict of interest.

Appendix A. Sensitivity analysis of the plate's distributed self-weight

In the present physical model, the gravitational driving force acting on the falling system is assumed to be entirely dominated by the central concentrated weight, while the distributed self-weight of the flexible plate itself is neglected. To rigorously validate the appropriateness of this assumption for lightweight-wing configurations, we conducted a sensitivity analysis by introducing a uniformly distributed gravitational load along the entire length of the plate.

We selected a representative baseline case with a concentrated weight of $G = 3$ and systematically varied the bending stiffness K. In the supplementary model, a distributed self-weight equivalent to 10 % of the concentrated central load was explicitly added to the structural governing equations. Figure 31 compares the quantitative kinematic outputs of this supplementary model against the original weightless-plate model. As shown in figure 31(a, b), both the normalised oscillation frequency f/f_{ref} and the terminal Reynolds number Re exhibit nearly perfect overlap between the two models across the entire investigated stiffness range. This comparison solidly confirms that, for the lightweight-plate regimes considered in this study, the inclusion of a minor distributed self-weight introduces negligible quantitative corrections. It does not alter the underlying force balance, the fundamental FSI kinematics or the mode transition boundaries. Therefore,

https://doi.org/10.1017/jfm.2026.11908 Published online by Cambridge University Press

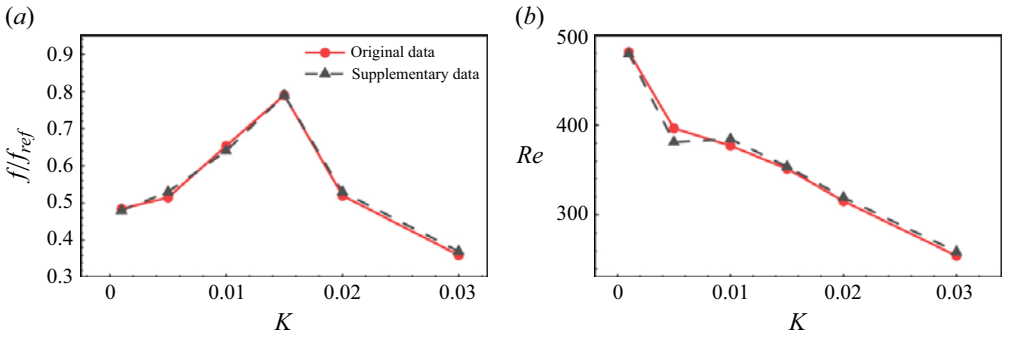


Figure 31. Quantitative comparison of the macroscopic kinematics with and without the distributed self-weight of the flexible plate at $G = 3$. (*a*) Normalised oscillation frequency f/f_{ref} and (*b*) Reynolds number Re as functions of bending stiffness K. The red circles represent the original model (neglecting plate self-weight), while the dark grey triangles represent the supplementary model where a distributed self-weight equivalent to 10 % of the concentrated load is explicitly considered.

neglecting the distributed self-weight is a robust, computationally efficient and physically sound abstraction for the present configuration.

References

Alben, S. 2010 Flexible sheets falling in an inviscid fluid. *Phys. Fluids* **22** (6), 061901.

Andersen, A., Pesavento, U. & Wang, Z.J. 2005 Analysis of transitions between fluttering, tumbling and steady descent of falling cards. *J. Fluid Mech.* **541**, 91–104.

Chen, S. & Doolen, G.D. 1998 Lattice Boltzmann method for fluid flows. *Annu. Rev. Fluid Mech.* **30** (1), 329–364.

Doyle, J.F. 2013 *Nonlinear Analysis of Thin-Walled Structures: Statics, Dynamics, and Stability*. Springer Science & Business Media.

Field, S.B., Klaus, M., Moore, M.G. & Nori, F. 1997 Chaotic dynamics of falling disks. *Nature* **388** (6639), 252–254.

Goldstein, D., Handler, R. & Sirovich, L. 1993 Modeling a no-slip flow boundary with an external force field. *J. Comput. Phys.* **105** (2), 354–366.

Huang, H., Wei, H. & Lu, X.-Y. 2018 Coupling performance of tandem flexible inverted flags in a uniform flow. *J. Fluid Mech.* **837**, 461–476.

Huang, W.-X., Shin, S.J. & Sung, H.J. 2007 Simulation of flexible filaments in a uniform flow by the immersed boundary method. *J. Comput. Phys.* **226** (2), 2206–2228.

Huang, W.-X. & Sung, H.J. 2010 Three-dimensional simulation of a flapping flag in a uniform flow. *J. Fluid Mech.* **653**, 301–336.

Iaccarino, G. & Mittal, R. 2005 Immersed boundary methods. *Annu. Rev. Fluid Mech.* **37**, 239–261.

Lau, E.M. & Huang, W.-X. 2021 Variations of flight patterns for falling flexible plates. *Phys. Fluids* **33** (8), 081904.

Lau, E.M., Huang, W.-X. & Xu, C.-X. 2018 Progression of heavy plates from stable falling to tumbling flight. *J. Fluid Mech.* **850**, 1009–1031.

Liu, K. & Huang, H. 2024 Dynamics of weighted flexible ribbons in a uniform flow. *J. Fluid Mech.* **990**, A11.

Mathai, V., Zhu, X., Sun, C. & Lohse, D. 2017 Mass and moment of inertia govern the transition in the dynamics and wakes of freely rising and falling cylinders. *Phys. Rev. Lett.* **119**, 054501.

Maxwell, J.C. 1852 Draft of paper on the descent of a body in a resisting medium. In *The Scientific Letters and Papers of James Clerk Maxwell* (ed. P.M. Harman), pp. 213–218. Cambridge University Press.

Peng, Z.-R., Huang, H. & Lu, X.-Y. 2018 Hydrodynamic schooling of multiple self-propelled flapping plates. *J. Fluid Mech.* **853**, 587–600.

Peskin, C.S. 2002 The immersed boundary method. *Acta Numerica* **11**, 479–517.

Rabault, J., Fauli, R.A. & Carlson, A. 2019 Curving to fly: synthetic adaptation unveils optimal flight performance of whirling fruits. *Phys. Rev. Lett.* **122** (2), 024501.

Tam, D. 2015 Flexibility increases lift for passive fluttering wings. *J. Fluid Mech.* **765**, R2.

https://doi.org/10.1017/jfm.2026.11908 Published online by Cambridge University Press

VINCENT, L., ZHENG, M., COSTELLO, J.H. & KANSO, E. 2020 Enhanced flight performance in non-uniformly flexible wings. *J. R. Soc. Interface* **17** (168), 20200352.

WANG, S. & ZHANG, X. 2011 An immersed boundary method based on discrete stream function formulation for two-and three-dimensional incompressible flows. *J. Comput. Phys.* **230** (9), 3479–3499.

WILLMARTH, W.W., HAWK, N.E. & HARVEY, R.L. 1964 Steady and unsteady motions and wakes of freely falling disks. *Phys. Fluids* **7** (2), 197–208.

XU, C., LIU, X., LIU, K., XIONG, Y. & HUANG, H. 2022 A free flexible flap in channel flow. *J. Fluid Mech.* **941**, A12.

ZHANG, C., HUANG, H. & LU, X.-Y. 2020 Effect of trailing-edge shape on the self-propulsive performance of heaving flexible plates. *J. Fluid Mech.* **887**, A7.

https://doi.org/10.1017/jfm.2026.11908 Published online by Cambridge University Press